REVIEW

Plasmon-dominated photoelectrodes for solar water splitting

Guohua Liu,[abc] Kang Du,[b] Jinliang Xu,[d] Guang Chen,[c] Mingyan Gu,[c] Changping Yang,[e] Kaiying Wang*[be] and Henrik Jakobsen[b]

Converting solar energy into chemical fuels through photoelectrochemical water splitting is an important technology for renewable energy development. Plasmon resonance of metal–semiconductor structures promises a great improvement of the efficiency of solar energy conversion. The principal mechanism is believed to be the spectral wavelength overlap of the photon absorbance of the semiconductor and surface resonance bands of the metal. A fundamental understanding of their structure–properties relationship has to be fully exploited for further developing efficient water-splitting techniques. This review aims to summarize design principles of plasmonic photoelectrodes and to rationalize many experimental observations. We have examined popular metal–semiconductor systems that show remarkable water-splitting performance. Three groups of plasmonic photoelectrodes are discussed in terms of their configurations, such as planar thin films, nanowire/rod arrays as well as porous structures. The physical difference and structural relationships with their photoelectrochemical performance are highlighted.

[a]School of Energy and Power Engineering, Nanjing University of Science and Technology, Nanjing 210094, China

[b]Department of Micro and Nano Systems Technology, University College of Southeast Norway, Horten 3184, Norway. E-mail: Kaiying.Wang@usn.no

[c]School of Energy and Environment, Anhui University of Technology, Maanshan 243002, China

[d]State Key Laboratory of Alternate Electrical Power System with Renewable Energy Sources, North China Electric Power University, Beijing 102206, China

[e]Faculty of Physics & Electronic Science, Hubei University, Wuhan 430062, China

1. Introduction

Hydrogen generation through solar water splitting is one of the promising routes to meet growing energy demands. Since water-splitting using a TiO_2 photoelectrode was reported, many efforts have been made to design efficient photoelectrodes.[1,2] A large number of oxide materials have been explored as light absorbers and electrode materials.[3,4] These oxides are promising materials due to their chemical stability in aqueous environments, affordability and easy availability. However, the known oxide materials and structures have not been able to

Guohua Liu received PhD in Engineering Thermophysics from the Chinese Academy of Sciences in 2010. He obtained his 2nd PhD in Micro and Nanosystems Technology at University College of Southeast Norway (HSN), 2013. He was a professor of Power Engineering at Anhui University of Technology and a Postdoc at HSN from 2013 to 2016. He is currently a professor of Renewable Energy at Nanjing University of Science and Technology. His research interest centers on the development and assembly of nanostructured materials for energy applications.

Kaiying Wang received PhD in condensed matter physics from the Institute of Physics, Chinese Academy of Sciences in 1995. He had been a postdoc at University of New Orleans, USA. He joined University College of Southeast Norway in 2007 as an associate professor and was then promoted as a professor in 2010. His research interests focus on micro-fabrication and nanotechnology, functional thin films, magnetic and superconductive materials, nanostructure characterization and nanodevices for environment and energy applications.
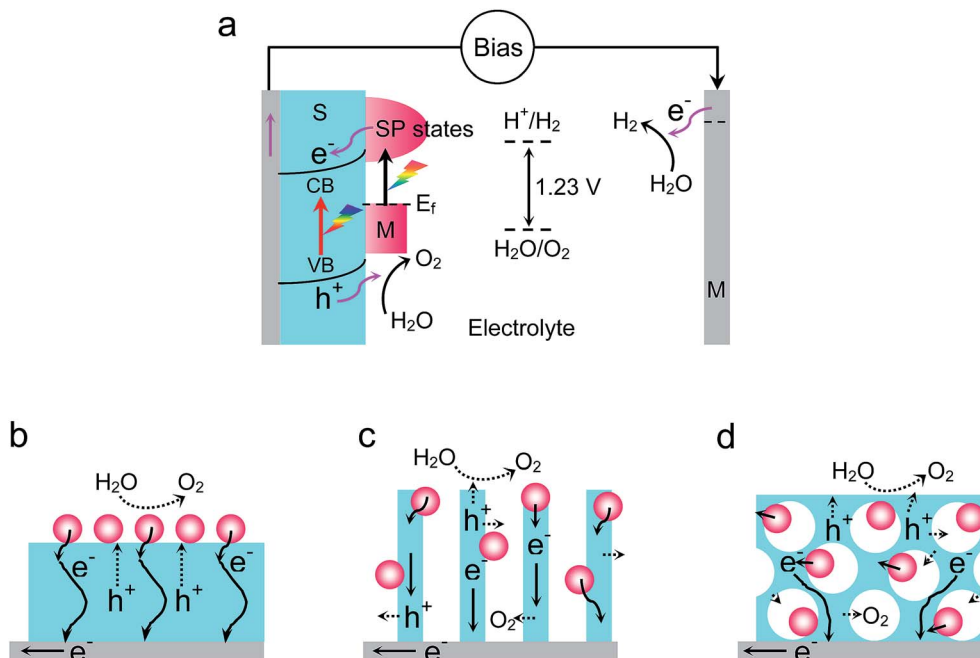
Fig. 1 (a) A photoelectrochemical process with a plasmon–semiconductor photoanode responding to visible light. Charge transport in (b) planar thin films, (c) nanowire/rod arrays and (d) porous structures.

satisfy both requirements of high energy-conversion efficiency and long-term stability. The crucial obstacles limiting the performance are the poor light-harvesting properties and high recombination rate of photo-excited charge carriers.

Attempts to address these issues focus on engineering material structures to enhance light absorption while shortening the travel distance of carriers to their surface. Surface texturing has been used to improve light trapping by reducing light reflection.[5] Nanostructure engineering has been employed to increase the exposure of active sites and reduce bulk recombination.[4] Crystallization is a good way to control the electronic structures for increasing carrier concentration and mobility.[6] Elemental dopants have been used to improve water-splitting efficiencies through a variety of doping effects, such as electrical conductivity enhancement, intra-band gap state formation and band gap narrowing, while the dopants or impurity sites act as recombination centers.[3] Band modification with small bandgap semiconductors or sensitization with organic dyes is a promising approach to extend light absorption.[3] Nevertheless, it creates undesired defects at the interfaces or is limited by the poor stability of the sensitizing agents.

Functionalization of light-absorbers with plasmonic metals is the best strategy because of the feasibility of increasing light harvesting and facilitating charge separation.[7] The plasmonic metals initiate surface plasmon resonance (SPR) in response to visible light and localize the electromagnetic energy to their surfaces.[8,9] The interaction of metals with their adjacent semiconductor allows for an enhanced generation of electron–hole pairs in the near surface region.[10] The SPR enhancement depends on the intensity of local electromagnetic fields as well as the surrounding environment. By engineering plasmon-dielectric structures, photons can be trapped and concentrated into a thin dielectric layer and consequently enhance the intensity of electromagnetic fields and the absorption.[11,12] However, how to construct plasmon–semiconductor structures with the desirable stability and high efficiency still remains a challenging goal.

In this work, we highlight the fundamental mechanisms of plasmonic enhancement for photoelectrochemical water splitting, followed by a brief remark on structure design and classification. A series of nanostructured plasmonic photoelectrodes (PPEs) including planar thin films, nanowire/rod arrays as well as porous structures (Fig. 1) are then extracted from the literature to

Henrik Jakobsen received his Cand. Real. Degree from University of Oslo in 1969, Norway and he was one of the co-founders of SensoNor AS in 1985. He joined the faculty at University College of Southeast Norway in 2002, where he was appointed as professor and head of the Department of Micro and Nanosystems Technology (IMST). He was elected as the Chairman of the Board of the industry cluster project "Norwegian Centre of Expertise – Micro- and Nano Technology" (NCE-MNT) in 2006 and now he is an Emeritus Professor at HSN. His current research interests focus on micro/nano-devices fabrication and commercialization.

illustrate the conceptual development. Independent plasmon-enhanced effects in different types of nanostructures are differentiated from each other by analyzing the material properties, structural configuration and band diagram of the electrodes.[13] We simultaneously examine the physical explanations with focus on understanding their structure–property relationships. Finally, the report concludes with a summary on the achievements and a few perspectives on the remaining challenges.

2. Fundamentals of plasmonic water splitting

2.1. Physical mechanisms

Different mechanisms have been proposed for plasmonic water splitting (Fig. 2),[12,14–19] which include (i) direct hot-electron transfer (DET), (ii) local enhancement of electromagnetic field (LEF), (iii) plasmon resonance energy transfer (PRT), (iv) plasmon-heating effect, (v) far-field light scattering and (vi) dipole–dipole coupling reaction. DET refers to injection of hot electrons from metals into the conduction band of semiconductors or direct reduction of water to hydrogen.[20] LEF strengthens light absorption and increases the generation and separation rates of charge carriers over the composite. PRT occurs when the resonance energy of plasmon oscillation is transferred from the metal to the neighboring semiconductor via a dipole–dipole interaction. This effect allows for charge generation below or near the semiconductor bandgap thanks to overlapping of the plasmonic resonance and bandgap. Plasmonic heating is a photothermic process resulting from the decay of LSPRs through phonon–electron relaxation, and subsequently the gained energy of mobile carriers turns into heat.[21,22] Light scattering on plasmonic crystals with a high *albedo* extends the photon-traveling path in photoactive materials. Plasmon oscillation induces fast-varying dipoles. The dipoles polarize molecules for better adsorption and thus increase their local concentration and catalytically active centers.

Apart from the above-mentioned effects, other mechanisms such as metal catalytic effect and quantum tunneling effect may also contribute to the performance. It is a challenge to determine the dominant mechanism in different situations since each effect has some requirements.[14,23] For instance, metals simultaneously serve as light absorbers and active catalytic sites in direct photocatalysis. The catalytic reactions are initiated directly on the surface of plasmonic metals.[24,25] In indirect catalysis on metal–semiconductor structures, synergistic effects of plasmonic metals and photoactive semiconductors are used for hydrogen generation.[10] Light-absorption properties of the materials together with their configurations determine the photoelectrochemical (PEC) performance. For a specific system, DET and PRT may function in a parallel manner or only one of them may be responsible for the enhancement. The preliminary requirement for DET is direct contact between plasmonic sensitizers and conductive materials. Isolation of plasmonic components with an insulator prohibits direct electron transfer. Light scattering properties of plasmonic components depend on the material, size and shape of the components. For a spherical metal nanoparticle (NP), the scattering increases with its size while the absorption decreases, denoting that the size of NPs can be tuned for maximum solar energy harvesting.

2.2. Design principles

Four aspects should be considered when designing a target SPR system.[26] The first is to determine the supporting semiconductor with/without insufficient light absorption and thus can benefit from plasmonic enhancement. The insufficient light absorption has two meanings. In one case, the absorption is inadequate since the semiconductor thickness is less than the absorptive depth. Plasmonic metals in this situation are employed to collect photons that would penetrate the semiconductor film if no metal particles are present. In another case, the light absorption occurs in an undesirable location, such as in the bulk volume of the semiconductor instead of the space-charge region at the interface. Besides harvesting photon energy, metal NPs in this case mainly serve to transfer the obtained energy to the neighboring semiconductor. Second, photoexcitation triggers the interplay of plasmon resonance and semiconductor excitation. Resonance coupling between them must be examined to ensure efficient energy transfer.[23] To determine the efficiency of energetic coupling, the light-absorption spectrum of the materials can be used to predict the spectral overlap of oscillation frequencies. The third concern is the physical contact states between the materials. Metal NPs have different contact states with the semiconductor.[27] An appropriate contact interface with the local environment would extend the light absorption spectral range while improper contact induces trap states at the interface, resulting in recombination and Fermi level pinning. These
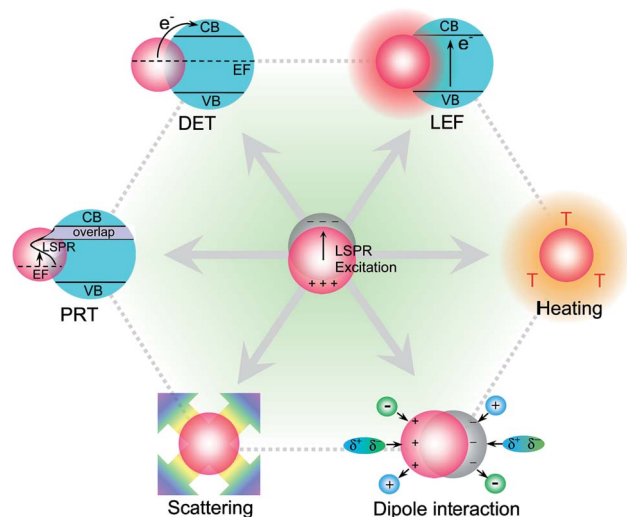

Fig. 2 Physical mechanisms involved in plasmonic water splitting: direct hot-electron transfer – DET; local enhancement of electromagnetic field – LEF; plasmon resonance energy transfer – PRT; plasmonic heating; far-field light scattering and dipole interactions. LSPR – local surface plasmon resonance. Adapted from references.[12,14,15,17,18]
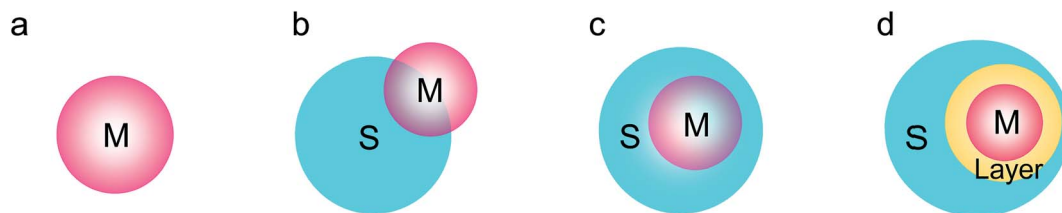
Fig. 3 Classification of plasmon–semiconductor structures. (a) Pure-metal form, (b) embedded form, (c) buried form, and (d) isolated form. Adapted from reference.[14]

contact states can be controlled and optimized through a fabrication process. The last consideration is the work function of the metal and its Schottky barrier at the interface. The barrier height determines the amount of the majority carrier that flows from the semiconductor to the metal. A design principle is to maximize the Schottky barrier height as much as possible, *e.g.* by using tiny metal NPs or isolating metal particles with an insulator layer.

To maximize charge collection, an appropriate contact pattern and a nanostructured semiconductor have been designed to enhance the efficiency. The contact pattern describes whether the plasmon metals are in direct touch with photoconductive materials or/and surrounding reactants.[11,14] In this regard, PPEs can be classified as shown in Fig. 3. The pure metal form refers to the reaction that depends only on the surface plasmon resonance of metal nanostructures (direct catalysis). The embedded form has metal NPs partially mounted on the photoconductive material with an electrical link, and is partially exposed to the neighboring electrolyte. The buried form presents a pattern without exposure to the electrolyte, and the metal NPs are completely buried into the photoconductive material. In the isolated form, metallic NPs are separated from the semiconductor film by a different dielectric layer so that no direct connection exists between the metals and the semiconductor. A variety of nanostructures including planar particle films, nanowire/rod arrays, nanotubes and porous structures have been adopted as supporting semiconductors for the metal NPs. Planar semiconductor films have a limited surface area

and suffer from serious recombination due to the repeated electron scattering/trapping at grain boundary sites. One-dimensional arrays possess merits such as vectorial charge transport, decoupling orientation for photon harvesting and carrier transfer. Porous structures offer large surface areas that extend the light responsive region and enhance light absorption, facilitate charge separation and reactant accessibility. We elaborate these three types of plasmonic structures and their corresponding PEC performances in the following sections.

3. Structures and performance of plasmonic photoelectrodes

3.1. Planar thin films

3.1.1. Embedded form. Recent advances in deposition techniques have made it easy for coating metal NPs onto the surfaces of semiconductor thin films to create Schottky junctions. The Schottky barriers are central building blocks for harnessing hot carriers. In this scenario, only hot-electrons with sufficient energy to surmount the Schottky barrier can climb up to the conduction band of the semiconductor. Direct injection of hot electrons from plasmonic metals to the adsorbed water molecules opens up a new way to fully harvest hot carriers with diverse energies.[25] Direct hot-electron injection has been observed in a thin film photocathode (Au NPs/NiO$_x$/Al), in which the carrier separation is facilitated by a transport layer NiO$_x$.[28] The thin film NiO$_x$ serves as a wide bandgap spacer layer
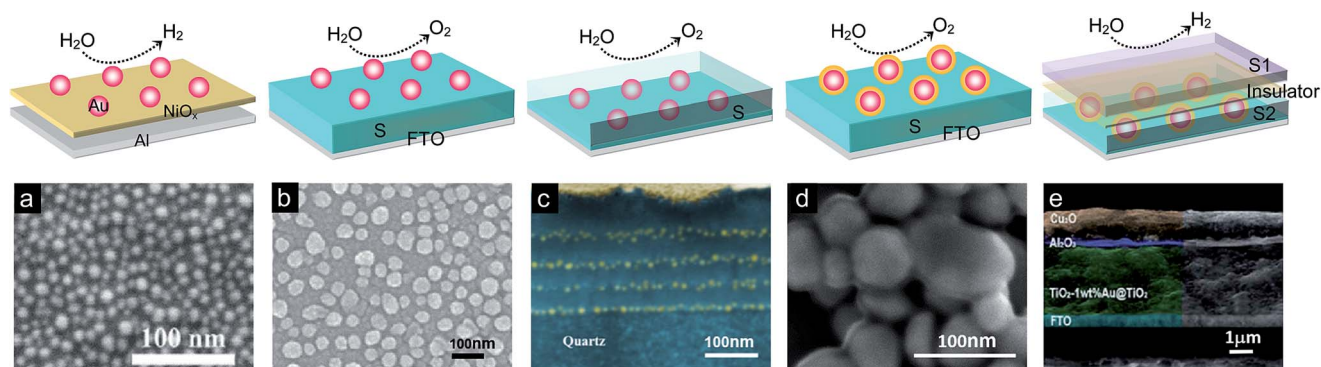
Fig. 4 Configurations of metal NPs on planar thin films: (a) direct plasmon-driven photocathode. Reproduced with permission.[29] Copyright 2015 American Chemical Society. (b) Plasmon-embedded film. Reproduced with permission.[31] (Copyright 2014 Elsevier). (c) Buried and (d) coreshell NP film photoanodes. Reproduced with permission.[38,48] Copyright 2011 American Chemical Society and Copyright 2014, Wiley-VCH. (e) A sandwich-structured film photocathode. Reproduced with permission.[56] Copyright 2015 Royal Society of Chemistry.

between Au NPs and the back reflector Al (Fig. 4a). The layer thickness can be adjusted to achieve maximum absorption. A pronounced photocurrent of 25 μA cm^{-2} was observed for 30 nm diameter Au NPs on top of a 40 nm thick NiO_x film, while only 0.250 μA cm^{-2} could be achieved without Au NPs.[29] The major factors contributing to this large photocurrent include enhanced light absorption of the structure by an optical impedance matching design, effective charge separation through the transport layer as well as efficient hot-electron injection from Au NPs to water molecules.

Plasmonic metals play a key role in photoelectrodes in which the resonance wavelength and localized SPR intensity are a function of the size or shape of the metal structures. By controlling the synthesis and assembling metal nanostructures, it is possible to construct PPEs with a wide solar spectrum response.[30] The size of gold NPs on TiO_2 photoelectrodes can be tuned from 30, 80 to 220 nm by thermal annealing of Au films with various initial thicknesses (5, 10, 20 nm). After annealing, the continuous metal film segregates into nanoparticles (Fig. 4b). The photocurrent density of the prepared electrodes increases from 1.38 μA cm^{-2} for the Au NPs of 30 nm to 2.23 μA cm^{-2} for the NPs of 80 nm, and then decreases to 1.47 μA cm^{-2} with further increase in the diameter to ~220 nm, while the pristine TiO_2 film produces an ultra-small current density of 0.03 μA cm^{-2}.[31] This confirms that there is an optimal initial Au film thickness at which the current density could be improved significantly. Au:WO_3 photoanode thin film was also prepared with various concentrations of cubic nanocrystalline Au. The cubic structures are formed with the size of 29–52 nm.[32] The highest photocurrent was observed for 1 mol% Au sample, with a hydrogen production rate of ~3 μmol h^{-1}. Another study further demonstrates that the optimized content of Au NPs with a diameter of 10 nm on WO_3 is 1.2 wt%. The electrode presents a high photocurrent of 0.44 mA cm^{-2}, which is about quadruple that of a WO_3 electrode.[33]

To distinguish the plasmonic effects, Au NPs with diameters ranging from 10 to 80 nm have been anchored on $BiVO_4$ thin films as photoelectrodes for solar water splitting.[34] Enhanced photocurrent densities are observed for all the films after adding Au NPs. A higher RET effect is observed at larger off-normal irradiation angle, while the effect of hot-electron injection is weak since the interband excitation of $BiVO_4$ is unfavorable for hot-electrons accumulation. The resonant photon scattering effect plays an important role when the Au NP size is greater than 60 nm. The maximum enhancement factor is reached for 20 nm and 30 nm Au NPs, resulting in a ~100% increase in photocurrent density. The evolution rates of H_2 and O_2 with the 30 nm Au NPs/$BiVO_4$ photoanode are 13.5 μmol h^{-1} cm^{-2} and 6.6 μmol h^{-1} cm^{-2}, respectively. This is due to the pronounced overlap of the resonantly amplified electric near-field with the inter-band excitation in $BiVO_4$.

Bimetallic particles are an alloy of two metals with complementary properties. When rationally synthesized and assembled, they can cause significant improvement of the photocatalytic properties.[35,36] A planar TiO_2 photoanode decorated with Au–Ag alloy NPs has been prepared using a reactive magnetron co-sputtering method.[37] The uniformity of the alloy

particles has been verified by UV-visible spectroscopy as well as binding energy shifts in XPS. Scanning electron microscopy shows that the diameter of the alloy particles is about 40 nm on the surface. Photoresponse measurements confirm a 30% enhancement of the photocurrent in the presence of alloy metals, and a 50% reduction of charge transfer resistance. Such performance mainly comes from the adjustment of the Schottky barrier height at the TiO_2/metal alloy interface. The work function of the alloy is decided by the composition of Au (~5.4 eV) and Ag (~4.5 eV). High silver content reduces the barrier height and increases the energy of hot electrons, and thus facilitates charge transfer from the metal alloy to TiO_2.

3.1.2. Buried form. In this pattern, all surface regions of the metal NPs have direct contact with the semiconductor materials, which will induce a large Schottky junction and fast charge transport. Although metal NPs act as electron sinks under UV irradiation, they would be saturated after they accumulate sufficient charges. The accumulated charges have no channel to escape in this situation, except for slow diffusion across the surrounding interface. Planar multilayer Au/TiO_2 has been prepared by depositing Au NP arrays with each layer being isolated by TiO_2 (Fig. 4c). The gold NP arrays were obtained by evaporation of thin film Au on TiO_2/quartz, and the film was then converted into NP arrays through a thermal annealing process.[38,39] The Au buried electrode exhibits a photocurrent of 0.35 μA cm^{-2}, which outperforms that of the Au sitting on the TiO_2 electrode (1.1 μA cm^{-2}). Multilayer 3D Au-buried TiO_2 electrodes further improve the performance to 1.8 μA cm^{-2} because of enhanced light absorption. Simulation results illustrate that the electric field in the vicinity of the Au NPs is very intense, which increases the electron–hole generation and accelerates charge separation.

Plasmon-enhanced performance has been observed in a hematite film buried with Au NPs as well.[40] The photocurrent of the films in the presence of Au NPs is about 3 times higher than that of the pristine one. The light concentration and scattering effects of Au NPs excite a large amount of charge carriers in the neighboring hematite and thus provide superior water splitting ability. Thickness-dependent PEC activities show a greater improvement in thin hematite films (110 nm) in contrast to thicker films (350 or 650 nm). This is due to the short distance of charge transport and enhancement of the local electromagnetic field in the structure. The PEC efficiency also increases with the amount of Au NPs for the same thickness of film. Integrating plasmon metals with a p–n junction can reduce charge recombination by speeding up the transport of electrons and holes. An n-ZnO/p-Cu_2O/Ag film triple-junction electrode has thus been constructed with a 11 times increase of photocurrent to ~1100 μA cm^{-2} compared to that of the Cu_2O film.[41] This can be attributed to the optimal tandem-structure design, in which the plasmon resonance of the silver film and the heterojunctions harvest solar energy in a complementary manner, leading to the enhancement of charge generation.

3.1.3. Isolated form. Considering the stability of metallic NPs in photoelectrodes, surface passivation is indispensable. After high temperature annealing of the electrode, the coating layer offers good thermal and chemical stability, which may

provide additional functionality, such as conductivity or mechanical reinforcement. There are three kinds of spatial configurations for isolated structures. Firstly, both core and shell are active components. The metal core with a conductive semiconductor shell is dispersed on a planar substrate, such as $Ag@TiO_2$ core–shell NPs synthesized by a hydrothermal method on an indium tin oxide planar substrate (ITO).[42,43] They showed characteristic absorption under visible light owing to the SPR of metal cores. The conductive shells enable charge accumulation because of the formation of Schottky barrier band bending at the interface as well as the transfer of photoelectrons from the surface of metal cores to the conduction band of the semiconductor shells. The obtained $Ag@TiO_2$ NP film exhibits strong light absorption and photoresponse in the wavelength range of 300–800 nm with an obvious band at 450 nm. Its photocurrent is much larger than that of the pristine TiO_2 film, whether under UV or visible-light irradiation. Au NPs have also been examined as the core but showed trivial enhancement in the absorption of TiO_2 due to the mismatch in the wavelength peak of plasmon resonance with the absorption band of TiO_2.[44,45] Nevertheless, $Au@TiO_2$ NPs anchored at the $CuWO_4$–electrolyte interface or at the $CuWO_4$ back contact were studied for PEC water splitting.[46] Incident photon-to-current conversion efficiencies (IPCEs) of the two samples increased about 6.0 times and 1.2 times, respectively. Au NPs with a 2 nm TiO_2 shell placed on a 200 nm $CuWO_4$ film increase the water-splitting photocurrent to 0.1 mA cm^{-2}. Benefits of the core–shell NPs at the $CuWO_4$/electrolyte interface include improvement of the surface catalytic properties, excitation of more charge-carriers in the space charge region and thus reduction of charge recombination.

Maintaining small NPs in a dispersed state is difficult, because of their high tendency of transport and agglomeration. An effective method for solving this problem is to coat the particles with a monolayer of polymer. In this case, the core is the active element and the shell works as a protector. Polymer coating does not affect the optical properties of the core because of its transparency. It also protects the electrical and optical properties of the material from environmental disturbances. The most common polymers used to stabilize plasmonic metals are polyvinylpyrrolidone and polyoxometalates. Ag nanocubes encapsulated by polyvinylpyrrolidone have been synthesized and then mixed with N-doped TiO_2 NPs.[47] This organic stabilizer molecule plays an important role in isolating a metal from semiconductor particles and avoiding backward charge transfer from TiO_2 to the metal. The sample presents one order enhancement of photocurrent to ~2.5 μA cm^{-2} as compared to the N-TiO_2 sample. Like the organic capping ligand, inorganic polyoxometalates also can be irreversibly adsorbed onto metal NPs (Fig. 4d).[48] Protecting Au NPs with polyoxometalates opens a new way to reduce recombination centers by the repulsive effect exerted on their ionic charges. The induced plasmon and catalytic effect of Au@polyoxometalate particles on thin film WO_3 leads to a large increase of the photocurrent to ~1.8 mA cm^{-2}, which is about twice as large as that of bare thin film WO_3.

Another strategy is to design plasmonic catalysts that have active nanoparticle cores protected by insulating silica shells. Silica is the most chemically inert material available. Silica coating blocks the core surface without interfering in the redox reaction and reduces the bulk conductivity. It can also be used to modulate the position and intensity of the surface plasmon absorbance band since silica is optically transparent. This insulating layer can be sandwiched between a metal core and a semiconductor layer, which protects the semiconductor against corrosion, and prohibits hot-electrons from crossing over the contact interface.[49–52] In this case, the associated mechanisms such as LSPR sensitization effect, electron transfer and Schottky junction are no longer effective. Besides, the insulating coating cuts off electric connections between the materials, so the enhancement effects are attributed to the increased photocurrent instead of photovoltage.[53] Thomann *et al.* have studied photocurrent enhancement of $Au@SiO_2$ NPs, which are buried in or embedded on an α-Fe_2O_3 thin film.[54] The Au NPs of diameter 50 nm are coated with a 10 nm silica shell and the thickness of the α-Fe_2O_3 thin film is about 100 nm. The pristine thin film produces a photocurrent of 0.1 mA cm^{-2}, while the photocurrent of $Au@SiO_2/Fe_2O_3$ increases ~11 and 20 times for the buried-in and the embedded-on samples, respectively. In addition, close matching of the peak positions is observed by comparing the photocurrent-enhancement spectra with the absorption spectra. This firmly indicates that the photocurrent enhancement is attributed to the LSPR of the $Au@SiO_2$ NPs. Photocurrent enhancement was also detected by modification of $BiVO_4$ film with $Ag@SiO_2$ core–shell NPs.[55] Optical absorption and catalysis are two contributions to this enhancement. The improved light absorption is triggered by the surface plasmonic resonance of Ag NPs, while the electrocatalytic activity of the core–shell NPs contributes to the catalytic enhancement.

$Au@TiO_2$ plasmonic NPs and p-Cu_2O/Al_2O_3/n-TiO_2 junction have been designed as a hybrid electrode (Fig. 4e).[56] The insulating Al_2O_3 layer was inserted between TiO_2-1 wt% $Au@TiO_2$ and Cu_2O to promote charge separation. The fundamental mechanism of the photoelectrode can be deduced based on IPCE measurements (Fig. 5a). The IPCE spectra of Cu_2O approaches zero at 620 nm, which results in a bandgap of 2.0 eV. Compared with the TiO_2-P25/Cu_2O photoelectrode, IPCE spectra of the above photoelectrode exhibit enhancement both in the UV and visible-light regions. Based on these observations, we can infer that scattering and plasmon-induced resonance transfer effects play a role in the phenomenon (Fig. 5b). Of the various sizes ~37, 70, 100, and 120 nm examined, the PPE with 120 nm Au cores not only enhances light absorption but also accelerates charge separation with photocurrent density of ~4.34 mA cm^{-2}, which is 20 times enhancement compared to the TiO_2/Cu_2O electrode. This high photocurrent is related to enhanced surface-scattering as well as effective separation of charge carriers through the insulating layer.

3.2. Nanowire/rod arrays

3.2.1. Metal nanorods/dots. Au nanorods (NRs) are elongated nanostructures with distinguished optical properties. Depending on their shape anisotropy, gold NRs exhibit two plasmonic modes. A transverse plasmon resonance band at
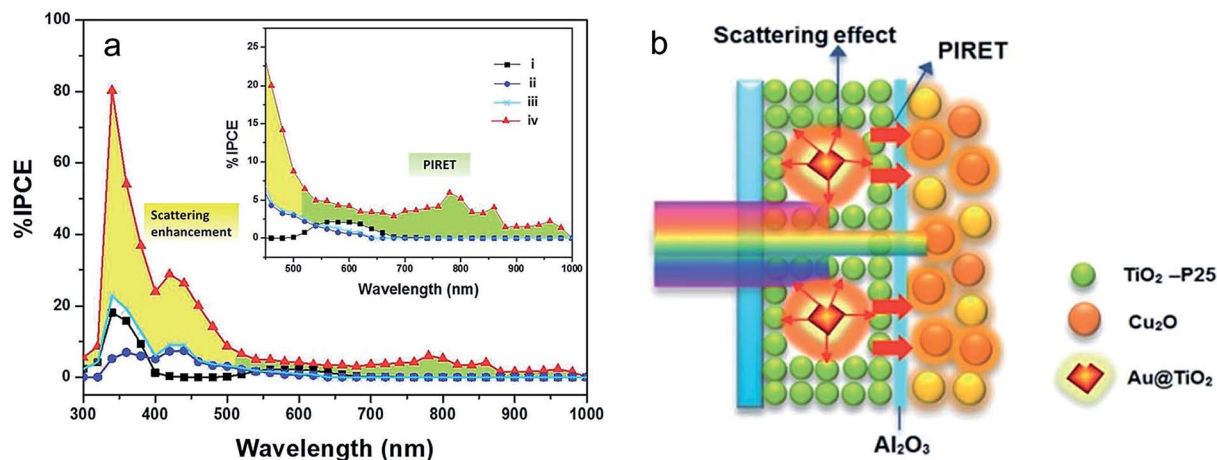
Fig. 5 (a) Incident-photon-to-current efficiency spectra of (i) FTO/TiO$_2$-1 wt% Au@TiO$_2$ (120 nm), (ii) FTO/Cu$_2$O, (iii) FTO/TiO$_2$-P25/Cu$_2$O and (iv) FTO/TiO$_2$-1 wt% Au@TiO$_2$ (120 nm)/Al$_2$O$_3$/Cu$_2$O photoelectrode. (b) Photon utilization on the photoelectrode. Reproduced with permission.[56] Copyright 2015 Royal Society of Chemistry.

visible light of around 520 nm and a longitudinal plasmon resonance band at a longer wavelength that can be controlled by tuning the aspect ratio of the NRs.[57] In PEC water splitting, surface plasmon excitation on Au NR arrays is liable to generate

all the charge carriers for the redox reaction (Fig. 6a or b).[58–60] The cell works by irradiating an Au NR array shielded with TiO$_2$, forming a series of metal–semiconductor Schottky junctions. These junctions collect hot-electrons and then conduct them to
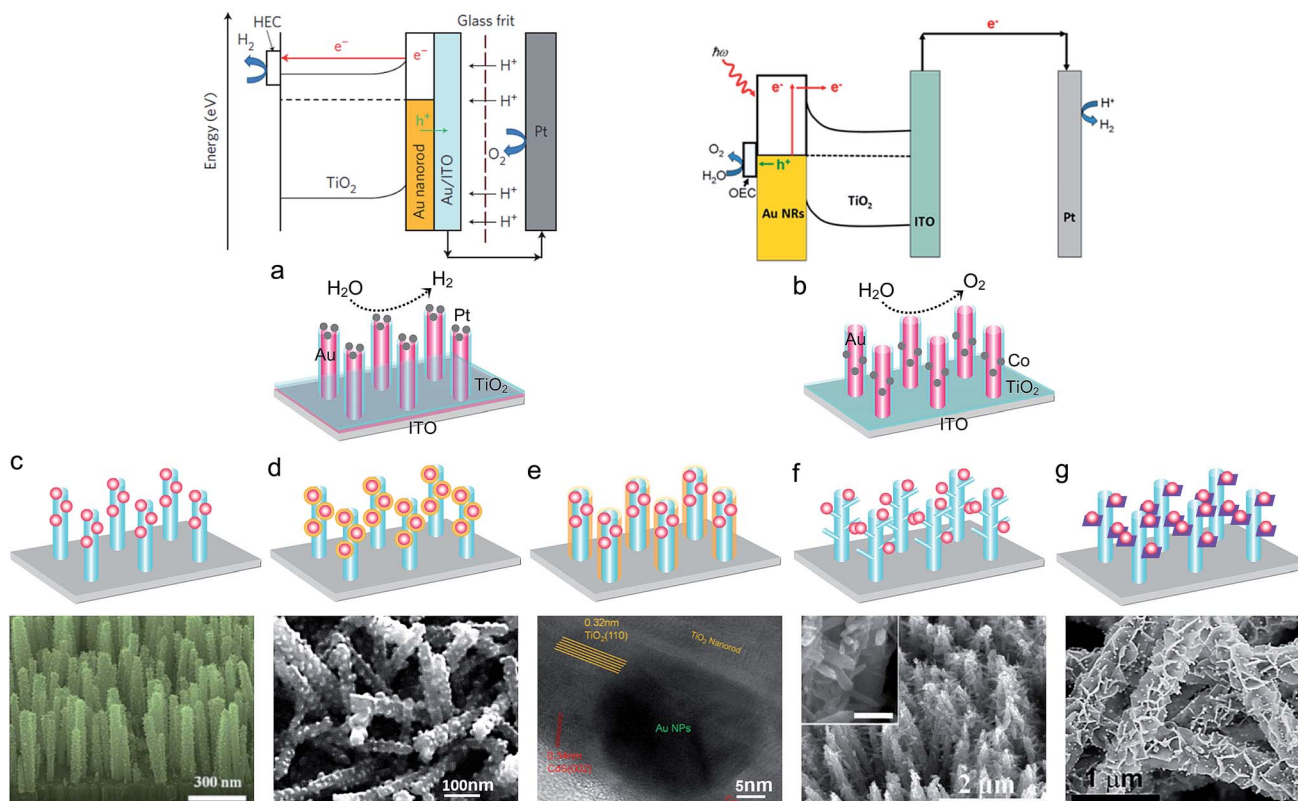
Fig. 6 Configurations of plasmonic elements on nanowire/rod arrays: (a) direct plasmon-driven photocathode and (b) anode. Reproduced with permission.[58,59] Copyright 2013 Nature Publishing Group and Copyright 2012 American Chemical Society. (c) Plasmon-embedded NWs, reproduced with permission.[64] Copyright 2016 Elsevier. (d) Coreshell NWs. Reproduced with permission.[71] Copyright 2014, American Chemical Society. (e) Plasmon-buried in coreshell NWs, reproduced with permission.[79] Copyright 2014 American Chemical Society. (f) Branched NWs and (g) nanoplatelet NWs. Reproduced with permission.[86,88] Copyright 2014 American Chemical Society and Copyright 2015 Wiley-VCH.

a counter electrode to perform the water reduction reaction. Meanwhile, the remaining positive holes on Au NRs are extracted to the oxidation catalyst for the water oxidation reaction (Fig. 6b).[59] The hydrogen generation efficiency shows 20 times improvement at visible wavelengths compared to that under UV illumination, proving that all effective charges can be derived from surface plasmon decay on the Au NRs. The size control of the plasmonic metal is critical for direct water splitting. A direct printing method has been used to print Au nanodot arrays onto ITO with dot size from 83 to 50 nm.[60] It was found that the water splitting reaction increases with decreasing the nanodot size. The photocurrent produced under visible light illumination is ~10–25 times that without visible light. TiO_2 coating on the nanodot array further increases the activity by 6 times.

Research on optoelectronic responses of organic molecules caused by SPRs of metals is significant for designing organic–inorganic PPEs. To design effective molecular-metal nanowire (NW) systems, Ag NWs coated with organic molecular perylene layers have been synthesized by an *in situ* surface reaction between silver nanowires and perylene.[61] The thickness of the perylene layer can be tuned by controlling the amount of initial perylene cation radicals. Strong coupling of the plasmon resonance of the silver NWs with the molecular exciton resonance leads to enhancement of fluorescence with a red shift in the Ag@perylene samples. Photocurrent measurements indicate that the perylene thickness is a key parameter. The optimal thickness is 5.8 nm and results in 16 times enhancement of the photocurrent. However, a simple mixture of Ag and perylene presents 6 times enhancement of the photocurrent, where hot-electron transfer from Ag NWs to perylene molecules in the organic-coating system plays a key role in the photocurrent enhancement.

3.2.2. Embedded nanowires/rods. Semiconductor NWs receive significant attention due to their distinct light absorption and scattering properties. NW arrays with different levels of anisotropy bring about strong polarization. The enhanced polarizability gives rise to multiple plasmon-resonance modes and red-shifts the peaks of optical resonance. Plasmon-induced enhancement in water splitting has been verified in diverse plasmon–semiconductor nanowires/rods (TiO_2, ZnO hematite, *etc.*). Au NPs ~20 nm have been photochemically grafted onto TiO_2 NWs.[62] The lifetime of hot electrons transferred to the TiO_2 conductive band is ~2 orders of magnitude longer than that of pristine TiO_2 under UV excitation. This is due to the Schottky junctions reducing the charge recombination, leading to a long excited-state of the transferred electrons. The long-living hot-electrons enable hydrogen evolution at a rate of 0.9 μmol cm^{-2} h^{-1} under visible light. The resonant absorption peak of gold NPs is around 550 nm. Manipulating the shape of the Au nanostructure is possible for utilization of other wavelengths of the solar spectrum.[63] Compared to pure TiO_2, Au NPs embedded on the TiO_2 NW array display an enhancement of photo-response under both UV and visible-light illuminations. An enhanced photoresponse of gold NRs decorated TiO_2 electrodes was observed in the visible-light region with a peak at 710 nm. More interestingly, a mixture of Au NPs and NRs doped TiO_2

NW array can extend the absorption range to a wide UV-visible region from 300 to 800 nm.

Silver or gold NPs can also be assembled onto ZnO NRs with a dense array (Fig. 6c).[64,65] ZnO NR arrays loaded with a diverse amount of Au NPs (~0.8%, 2.5%, 4.7%, 9.8%, 18.5%) have been studied for water splitting.[66] Pristine ZnO NRs show no photocurrent because ZnO is not excited under visible light. After decoration of a few Au NPs on the ZnO NR array, the photocurrent increases rapidly. The photocurrent increases as the Au concentration increases from 0.8 to 9.8%, achieving a maximum photocurrent ~0.3 mA cm^{-2}. Further increasing the gold-particle density reduces the photocurrent. The enhanced photocurrent with an increased Au concentration is due to the extended light absorption range and improved separation of charge carriers. However, excessive deposition would make Au NPs an additional center of charge recombination, and thus reduce the photocurrent. Recently, Au NPs positioned on the tip of ZnO NR arrays were *in situ* prepared by using a facile hydrothermal and photoreduction method.[65] The structure with 1.9% Au atomic ratio presents a high photocurrent of 9.11 mA cm^{-2}, with solar-to-hydrogen efficiency of 0.48%. This efficiency is 16 times greater than that of the pure ZnO NRs. The ZnO NW array modified by Ag NPs with a triangular shape shows enhancement in photoelectric energy conversion with a maximum conversion efficiency of 1.45%.[67] The photocurrent intensity is 3.1 and 10 times greater than that of Ag NPs decorated ZnO and as-grown ZnO NRs. This enhancement is ascribed to enhanced plasmonic hotspots on their sharp tips. ZnO NRs shielded with a silver film have been constructed on a polyethylene terephthalate (PET) flexible substrate to improve light harvesting.[68] The plasmonic effects are studied by varying the Ag film thickness to ~0, 5, 10, 20, 30, 50 nm. Compared with a flat nanorod structure, ZnO NRs with 10 nm silver film coating on a curved substrate ($R = 6.0$ mm) facilitate optimal light-harvesting. The short circuit current density is 0.60 mA cm^{-2}, with a photon-to-electron conversion efficiency of ~0.81%. Plasmonic effects of the metallic film, directional charge transport in the 1D NR surface together with enhanced light trapping through the bending substrate account for this performance.

The efficiency of water splitting is further studied by using Au NPs buried in hematite particle films and embedded on the surface of hematite NRs.[26] When Au NPs ~50 nm diameter are buried in a 31 nm compact hematite film, no obvious plasmon enhancement was observed due to the spectral mismatch between the plasmonic resonance band of the metals and the photoexcitation band of the semiconductor. However, improvement of spectral response was observed for the NR photoelectrode. This is due to plasmon-enhanced photon absorption and charge generation, and subsequent transfer of the energy gained to the hematite NRs. As such, the PPEs produce a photocurrent of 2.0 mA cm^{-2} in contrast to only 0.4 mA cm^{-2} of the buried one. To utilize both propagating surface plasmon and localized surface plasmon resonance, Li *et al.* developed a photoanode where hematite NR arrays were assembled inside gold nanohole arrays.[69] In this manner, the propagating surface plasmon of Au nanoholes captures

incident light at the energies above the hematite band edge. The transfer of resonance energy of the spectral overlap of photo-excitation harvests solar energy below the hematite band edge. The NRs serve as optical antennas for enhancing light absorption. As a result, the hematite NRs in Au plasmonic nanoholes give rise to 10 times enhancement of photocurrent.

Rational assembly of various plasmonic segments within a single NW assists in interfacial charge separation and transport. However, improper arrangement of the components with an undesired energy band would introduce unexpected energy-barriers at the interfaces and prohibit carrier transport. This has been verified in complex nanobamboo arrays (NBAs) that consist of various plasmonic-metals and semiconductor segments.[70] The ZnS–Ag–CdS–Au–CdSe NBAs produce a high photocurrent density of 8.57 mA cm^{-2}, while its opposite structure ZnS–Au–CdS–Ag–CdSe NBAs yields a photocurrent density of 2.22 mA cm^{-2}. This is because the former architecture has a designable cascade interfacial energy band. In particular, the silver Fermi level (-0.48 V$_{NHE}$) is higher than that of CdS and ZnS, producing ohmic contacts both at ZnS/Ag and Ag/CdS interface, which is advantageous for charge transport. The Fermi level of Au is $+0.42$ V$_{NHE}$, which is lower than that of both CdS and CdSe. Interfacial Schottky barriers are generated at both CdS/Au and Au/CdSe interfaces. However, due to the PRT effect, more excitons are generated in CdS segments, leading to increase in the carrier density. This enhances the conductance of CdS and realigns relative energy levels at the interface, resulting in a reduced barrier height. Therefore, electrons can cross over the height-reduced Schottky barrier. For the reverse structure, a notable barrier height of 0.87 eV is created at the ZnS/Au interface. Since there is no absorption spectrum overlap between ZnS and Au, the PRT effect between them is negligible. Without more excitation, neither can the carrier density in ZnS be increased nor can the Schottky barrier height be reduced. Thus, the electrons cannot cross over the Schottky barrier.

3.2.3. Coreshell nanowires. Coreshell NPs or NWs possess unique physical and chemical properties. Coating plasmonic NPs with a protective layer can improve their stability. Ag@Ag$_2$S coreshell NPs decorated TiO$_2$ NW electrodes have been observed with pronounced photoelectrochemical responses and stability (Fig. 6d).[71] The collective merits such as the visible light harvesting ability of Ag$_2$S, surface plasmon enhancement of Ag and fast charge transport in 1D NWs are responsible for the performance. Au@SiO$_2$ NPs have also been loaded onto the surface of TiO$_2$ NRs.[72] Compared with bare NR arrays, the core–shell NPs anchored on TiO$_2$ NRs show outstanding performance in water splitting, with IPCE increasing from 31% to 37%. This is attributed to the plasmonic resonance effect of the Au@SiO$_2$ NPs, which creates a strong localized electromagnetic field with spatially distributed intensity. Consequently, the excited charge carriers are easily separated in the neighboring region of TiO$_2$ NRs. By depositing Ag NPs with a 2 nm thick shell of Ag$_3$(PO$_4$)$_{1-x}$ on ZnO NR arrays, remarkable water oxidation was achieved with a photocurrent density 3.1 mA cm^{-2}.[73] The rate of O$_2$ evolution for the electrodes is $\sim$34 μmol h^{-1} with good stability for $\sim$10 h. This is due to the plasmonic effects of Ag

resulting in an increase of light absorption as well as enhanced charge generation rate in the nearby surface of ZnO NRs. Cu$_2$O nanowire networks decorated with Au@SiO$_2$ core–shell NPs have also been studied to investigate the plasmonic effect.[74] Introducing core–shell NPs into the Cu$_2$O NW network not only increases light absorption, but also creates an intense localized electromagnetic field to promote charge generation and transport. The cathode displays an increased IPCE at a wavelength of 550 nm to yield 3 times enhancement of the photocurrent that agrees well with the plasmon resonance band of Au NPs. Photoluminescence measurements combined with optical simulations reveal that the electromagnetic near-field enhancement is responsible for the enhancement of photocurrent.

There are two other types of plasmonic core/shell NWs. One of them is plasmonic metals embedded on the surface of core/shell NWs (Fig. 6e). This has been realized in Au decorated Zn$_x$Cd$_{1-x}$Se$_y$Te$_{1-y}$/ZnO core–shell NWs,[75] Au–ZnS/ZnO NWs,[76] Ag–polydopamine (PDA)/ZnO NWs[77] and Ag–conductive polymer-protected Si NWs.[78] After modification with 10 nm Au NPs, the Au–Zn$_x$Cd$_{1-x}$Se$_y$Te$_{1-y}$/ZnO NW array shows remarkable hydrogen-production ability by water splitting, $\sim$2.172 mmol g^{-1} without obvious degradation after three cycles in 12 h. The Au–ZnS/ZnO NW anode achieves a solar-to-fuel conversion efficiency of 0.21%, which is 2 times and 3.5 times that of Au–ZnO and pristine ZnO anodes, respectively. The results illustrate that the combination of semiconductor-heterojunctions with the SPR of plasmonic NPs has simultaneous merits of a broad absorption edge and high charge separation efficiency. To realize spatial distribution of the plasmonic NPs, polydopamine (PDA) has been proposed to help the decoration of ZnO NWs with silver particles. The obtained photoanode has superior light-absorption ability because of the plasmonic effect of the metal NPs and additional photon harvesting from carbonized PDA. Ag NPs also function as an electron sink, while the carbonized PDA shell acts as the stabilizer and separator, which facilitates charge transport and reduces charge recombination. Thus, a larger photocurrent of 1.8 mA cm^{-2} with a longer lifetime is observed in comparison with other reported Ag–ZnO anodes.

Another case is metal NPs buried in a core/shell NW structure. In CdS/Au/TiO$_2$ NRs, gold NPs buried between TiO$_2$ NRs and the CdS quantum dot (QD) layer undertake two functions in water splitting.[79] The gold NPs firstly function as an electron transfer mediator that promotes charge transport from CdS to TiO$_2$ when both materials are photoexcited at a wavelength of 525 nm. Secondly, the gold NPs act as a plasmon sensitizer at a longer wavelength of 725 nm where CdS is not active. The dual role of gold NPs gives rise to a high photocurrent density of 4.0 mA cm^{-2} under solar spectrum irradiation, with solar-to-fuel efficiency of $\sim$2.8%. Au NPs buried in organic–inorganic hybrid structures (e.g. polythiophene shell/Au/TiO$_2$ NW on an FTO substrate) have also been synthesized by hydrothermal and electrodeposition methods.[80] The as-prepared photoelectrode exhibits optimal photoelectric conversion efficiency of 0.11% and hydrogen production rate of 2.929 mmol h^{-1} m^{-2}. The enhanced water splitting is attributed to the transparent poly-thiophene shells acting as the photosensitizer and Au NPs

acting as both an electron-transport bridge and plasmonic sites. Similarly, CdS/Ag/ZnO NW photoanodes improve water oxidation, presenting a constant hydrogen evolution rate of ~155 μmol h^{-1} for 10 h. Even without bias, a hydrogen production rate of ~22 μmol h^{-1} is still observed.[81] The Al$_2$O$_3$/Au/Fe$_2$O$_3$ electrode shows 1.78 times photocurrent enhancement compared to that of the pristine Fe$_2$O$_3$ at a bias of 0.4 V.[82] Al film has also been proposed as a plasmonic element for achieving low cost and scalable electrodes. The thin film Fe$_2$O$_3$/Al/Si NWs theoretically produce photocurrent densities comparable to Fe$_2$O$_3$/Ag/Si NWs.[83] An expected photocurrent of ~11.81 mA cm^{-2} can be achieved by the photoelectrode with a 40 nm thick hematite layer.

3.2.4. Branched nanowires/platelets.

Constructing leaves and/or secondary branches on bare NWs is an effective way to improve charge collection efficiency and enhance the roughness. By assembling various functional materials, the structure is normally heterogeneous, and can also be homogeneous. A tree-like Ag/ZnO NW array has been prepared by a two-step electrodeposition process.[84] ZnO NWs act as the main trunk, while the silver nanocluster leaves are selectively anchored on top of the NWs. Under visible light irradiation, strong electromagnetic fields around the Ag nanocluster induced by SPR promote energy transfer to ZnO through hot-electron injection. The photocurrent of the electrode increases to 0.17 mA cm^{-2} at 1.23 V$_{RHE}$, corresponding to a photon-to-fuel efficiency of ~0.23%. Ag plasmonic nanoclusters on the top of Si microwires increase ionic or gas diffusion rates.[85] The onset potential of the cathode with a rough surface positively shifts by ~500 mV as compared to the Si microwire electrode. An optimized

photocurrent of −35 mA cm^{-2} at −1.0 V can be obtained by tuning the amount of Ag nanoclusters. These systems demonstrate that leaf-like plasmonic clusters deposited on a semiconductor trunk is a successful architecture for PEC application.

Compared with 1D NWs, 3D branched NWs offer an additional roughness factor. The increased roughness is advantageous to the loading of plasmonic NPs, which improves the light-harvesting efficiency. The gold NPs on branched ZnO NW photoanodes exhibit outstanding PEC performance in both UV and visible-light regions (Fig. 6f). The H$_2$ evolution rate of the electrode is ~19.6 μmol h^{-1} cm^{-2} with photoconversion efficiency reaching 0.52%.[86] This high efficiency is ascribed to hot-electron injection from excited gold NPs to branched ZnO NWs. Heterogeneous-branched Ag/Ag$_2$S/Ag$_3$CuS$_2$/TiO$_2$ NRs have also been constructed by successive ion layer adsorption/reaction followed by an ion-exchange method.[87] The heterostructures increase the charge collection efficiency and inhibit the recombination *via* light harvesting through multiphotosensitizers. By optimizing the quantity of the components, such structures exhibit a photocurrent of ~2.27 mA cm^{-2}, which is about 2 times larger than that of TiO$_2$ nanorods.

Two NPs with a small gap is a classic plasmonic model. In the gap region, electromagnetic fields are folded into a hot spot *via* plasmon-coupling interaction.[88,89] In this manner, inserting an ultrathin platelet into this hot spot, forming a dimer structure, can boost charge generation (Fig. 6g).[88,90–93] Au NPs sensitized ZnO nanorod@nanoplatelet (NR@NP) arrays have been prepared by a hydrothermal method following Au NP decoration. The coordination of the hierarchical structure and
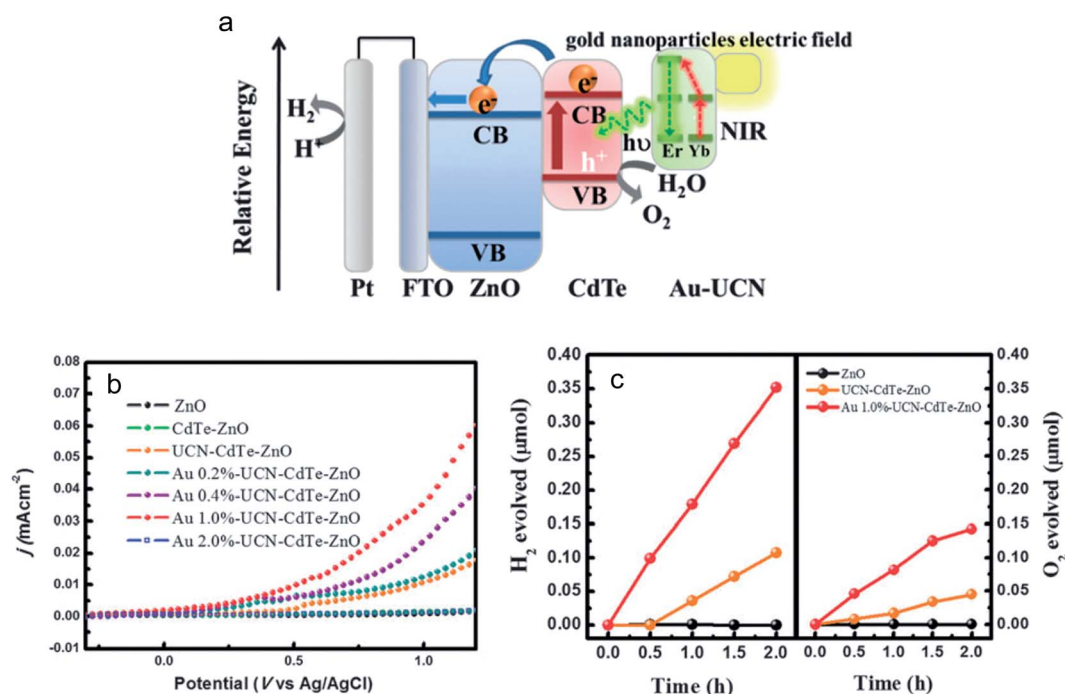

Fig. 7 (a) Energy conversion mechanism on the Au/UCNs/CdTe/ZnO NR photoelectrode. (b) Linear–sweep voltammograms and (c) gas evolution process of the photoanodes in 0.5 M Na$_2$SO$_4$ solution. Reproduced with permission.[91] Copyright 2013 Royal Society of Chemistry.

intensive electromagnetic field from plasmon-coupling enhances visible-light absorption and facilitates the exposure of active sites, thus increasing the charge generation rate. The structure exhibits exceptional water splitting properties, leading to a high photocurrent density of $\sim$1.47 mA cm^{-2}, much superior to those of ZnO NR arrays (0.89 mA cm^{-2}) and ZnO NRs@NPs (1.17 mA cm^{-2}).[92] The near-infrared-driven water splitting is further explored by using ZnO NRs decorated with CdTe QDs and Au plasmonic upconversion-nanoplatelets UCNs (Er^{3+}/Yb^{3+} co-doped NaY).[91] In this system, UCNs are used to harvest and convert NIR light to high-energy photons. The plasmonic resonance effect of Au is channeled to excite upconversion luminescence from UCNs, and the luminescence further excites the CdTe quantum dots to produce charge carriers (Fig. 7a). These long-lived carriers flow through the ZnO conductive band to the platinum counter electrode for hydrogen production, thereby producing the photocurrent. The photocurrent of Au-1.0 wt%/UCNs/CdTe/ZnO reaches $\sim$0.036 mA cm^{-2}, which is $\sim$3 times larger than that of the UCNs/CdTe/ZnO electrode (Fig. 7b). The system produces 0.18 μmol h^{-1} of hydrogen under 980 nm laser illumination (Fig. 7c), evidencing that water splitting had been achieved under near-infrared irradiation.

3.3. Porous structures

3.3.1. Nanotube arrays. Nanotube arrays show higher surface area than planar particle films. The porous channels with a high surface area enhance photon-absorption by multi-reflections and reactant adsorption. Precisely controlling the local position of metals outside or inside the pore surface of nanotubes is the main focus in the synthesis of plasmon-nanotube catalysts.[94] Gold NPs have been deposited on TiO$_2$ nanotubes (TNTs) via a seed-mediated approach.[95] The TNTs with Au NPs located outside wall surfaces are a disordered, porous scaffold. By tuning the size of the metallic particle to 20–100 nm, hot-electron injection enhances the photocurrent over a wide wavelength from 500 to 1000 nm. IPCE measurements indicate the largest photocurrent increase of $\sim$200 times at 700–730 nm wavelength. To decorate metal NPs onto inner pore surfaces of TNTs (Fig. 8a), a pulse electrodeposition or evaporation technique has been adopted to disperse Au NPs on ordered TNTs obtained by anodization.[96,97] In this way, surface plasmon resonance induced a strong electric field near the nanotube surface, which enhances the light-absorption of TiO$_2$ and thus boosts PEC activity. The photoanode exhibits 66 times enhancement in water splitting, producing a photocurrent of 0.3 μA.[97] However, the hot-electron injection from gold to TiO$_2$ is difficult owing to the unsuitable band energy alignment of the two materials. Inserting a proper electron mediator between them is a wise tactic to facilitate carrier transport. Au/reduced graphene oxide/hydrogenated TNTs (Au/RGO/H-TNTs) are thus synthesized via electrophoretic deposition of gold and graphene oxides onto H-TNTs. The hydrogenation process narrows the bandgap and improves the conductivity of TNTs. The plasmon resonance of gold NPs has a strong and broad visible-light harvesting ability. Moreover, the deposited RGO

films act as an efficient electron relay that accelerates hot-electron transfer. Thus, the obtained sample shows a prominent photocurrent of 224 μA cm^{-2} with a hydrogen generation rate of 45 μmol h^{-1}, much larger than that of the other references.[98]

Among various metallic nanocrystals (Au, Ag, Cu, Pd), silver is a suitable material since it has an appropriate energy-level arrangement and good photo-stability. Different methods have been attempted to load Ag NPs on TNTs. Ultrafine Ag NPs from 1.3 to 21.0 nm have been precisely controlled and uniformly deposited on TNT surfaces via the pulse electrodeposition route.[99] Strong plasmon resonance without the shielding effect of the silver crystals greatly improves the TNT performance for water splitting. The optimal size of the silver crystals is $\sim$2.5 nm, delivering a hydrogen generation rate of $\sim$124.4 μmol cm^{-2} h^{-1}. Ag NPs in the diameter of 5 nm have been decorated on N-TNTs by an electrochemical deposition method.[100] The carrier density of the sample is two orders magnitude higher than that of pristine TNT. Owing to the high generation rate of photocarriers and fast transport, the photoanode delivers a photocurrent of 0.14 mA cm^{-2}. This current is the highest one compared with the TNT, N-TNT and Ag/N-TNT samples. AgX (X = Br, I, Cl) silver halides are excellent photosensitive materials. TNTs sensitized with AgBr/Ag core–shell NPs have been synthesized via a successive ionic layer adsorption/reaction technique combined with a photoreduction method.[101] The synergy of visible light harvesting by the strong SPR and polarization field offered by the AgX core greatly enhances charge separation and transport. As a result, the samples display strong plasmonic response to visible light with photocurrent equal to 0.73 mA cm^{-2}.

Dielectric properties of the neighboring materials or environment have a key influence on the plasmon resonance frequency and intensity. Using high refractive-index materials in the surroundings would strengthen the plasmon resonance and induce a red-shift, which is advantageous to enhance the performance.[102] To unveil energy transfer mechanisms in metal–dielectric–semiconductor structures, a series of structural configurations of TNT backbones coated with Au, Al$_2$O$_3$, or both have been fabricated via photoreduction plus atom layer deposition methods. The plasmon-excited hot electron injection is dominant in the Au/Al$_2$O$_3$/TNT electrode (i.e., an insulating spacer in the middle, Fig. 8b), and the photocurrent generated is 0.5 mA cm^{-2}.[103] The Al$_2$O$_3$/Au/TNT electrode shows outstanding photoresponse and the best PEC performance, producing a photocurrent of 0.7 mA cm^{-2}. The Al$_2$O$_3$ coating in the latter case enhances the local electromagnetic field and reduces recombination, accounting for the difference in performance.

Semiconductor photonic segments possess strong light-harvesting ability due to slow-photon enhancement and multiple stop-band reflection among the segments. A plasmonic photonic segment has been assembled by using Au nanocrystals with a TNT photonic crystal layer (Fig. 8c).[104] Due to appropriate matching of the gold surface plasmon wavelength with the TiO$_2$ photonic bandgap, the increased SPR intensity boosts hot electron injection and thus enhances PEC
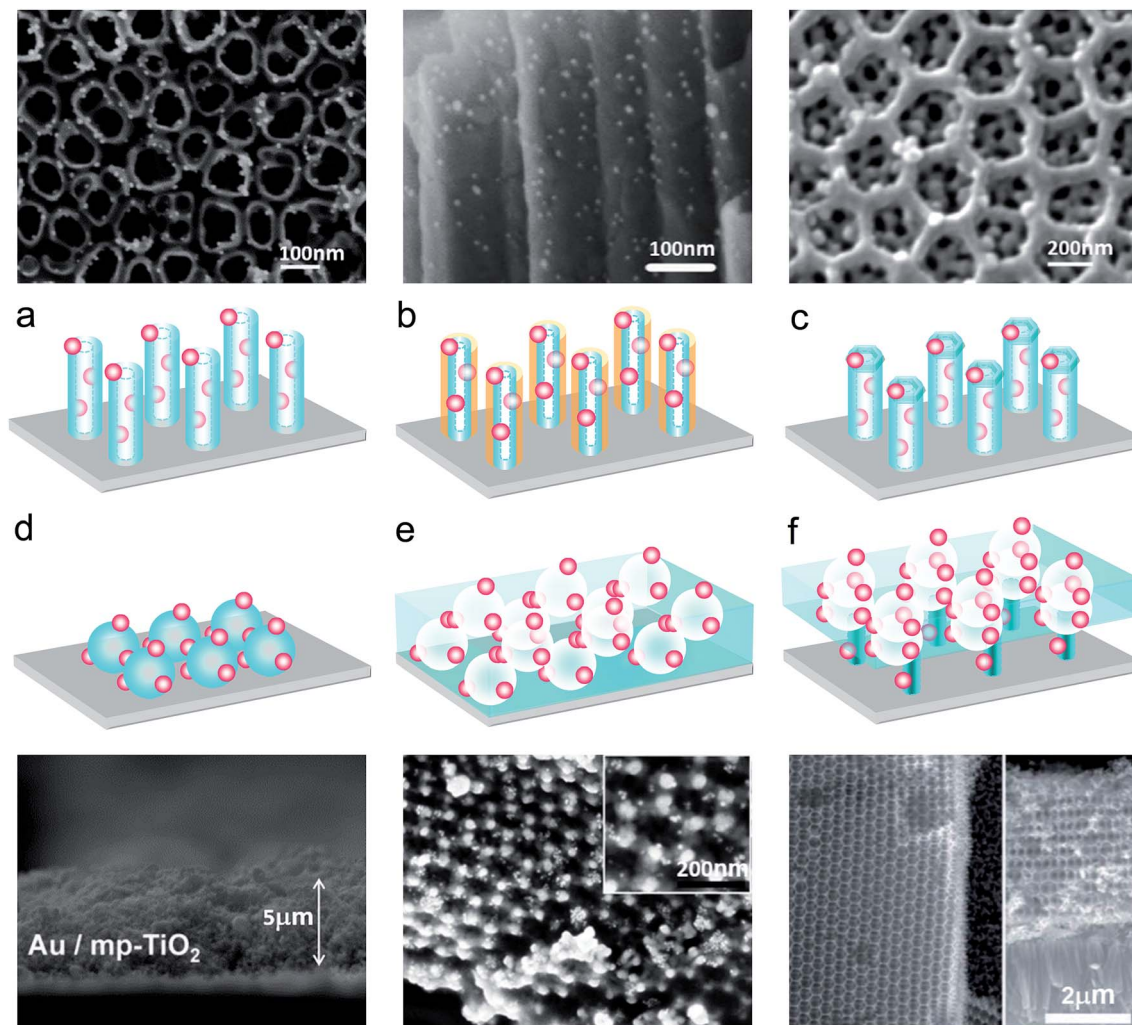
Fig. 8 Configurations of plasmonic NPs on porous structures: (a) embedded on nanotubes and (b) on coreshell nanotubes, reproduced with permission.[96,103] Copyright 2015 Elsevier and Copyright 2015 Wiley-VCH. (c) On nanotube photonic crystal, reproduced with permission.[104] Copyright 2013 American Chemical Society. (d) On a mesoporous layer, reproduced with permission.[107] Copyright 2014 American Chemical Society. (e) On an inverse opal structure and (f) on a dual-layer photonic crystal. Reproduced with permission.[111,112] Copyright 2014 Wiley-VCH and Copyright 2014 Royal Society of Chemistry.

water-splitting performance. The photonic composite delivers a photocurrent of $\sim$150 μA cm^{-2} under visible light. Gas evolution rates are 27.9 μmol h^{-1} for H$_2$ and 13.6 μmol h^{-1} for O$_2$, respectively. When the size of metal NPs becomes atomically small (<2 nm), and protected by a stabilizing ligand, they can be named "metal clusters". Metal clusters featuring peculiar atom packing have a quantum confinement effect, resulting in a band structure with discrete energy levels. Coupling gold nanocrystals and glutathione-capped Au$_x$ clusters with a TNT-photonic crystal framework greatly improves the visible-light PEC performance as compared with single and binary counterparts.[105] This is because Au nanocrystals functioning as electron relay mediators and the Au$_x$ clusters as the plasmonic sensitizer synergistically enhance light absorption and charge transfer.

3.3.2. Mesoporous structure. Photonic structures with ordered porous structures give rise to a photonic stop-band to

certain light frequencies. Arranging photoconductive materials in a porous structure offers a promising approach to tailor the spectral response of the material to match the plasmonic resonance spectra.[106] Loading both gold NPs and TiO$_2$ mesoporous NPs on a fluorine-doped tin oxide conducting substrate (Au/mp-TiO$_2$/FTO, Fig. 8d) shows that the mesoporous structure permits permeation of solution into the mesopores to reach the FTO surface. The fluorine-doped tin oxides with good conductivity promote long-distance charge transport with restricted back electron transfer to gold, enabling higher activity of the Au/mp-TiO$_2$/FTO (1.5 μM h^{-1}) than Au/mp-TiO$_2$/glass (0.75 μM h^{-1}). Furthermore, by tuning TiO$_2$ particle size ($\sim$15, 80, 250, 500 nm), visible-light activity was found to increase with a decrease in particle size.[107] Diverse amounts of Au NPs embedded on mesoporous TiO$_2$ have been further introduced to differentiate LSPR and catalytic effects.[108] Faster charge transfer kinetics demonstrate that the presence of gold particles

increases the catalytic performance of the photoelectrodes, while it is difficult to translate the plasmonic hot-electrons into photocurrent.

Inverse opals with long-range ordered pores can produce a periodic modulation of the refractive index in space.[109] By deposition of Au NPs onto TiO_2 inverse opals, the opal composite enhances photon-harvesting through the exposed large surface area for plasmonic loading, while the small pore areas are retained for liquid penetration. The strong plasmonic resonance of the gold NPs improves the photon-to-electric conversion efficiency. The anode induces a remarkable photo-current of 0.8 mA cm^{-2}, which is about 2.8 times higher than that of pristine inverse opal.[110] Photonic photoanodes are also fabricated through coupling of an inverse opal $BiVO_4$ with plasmonic gold NPs (Fig. 8e).[111] By synergetic coupling with the photonic Bragg resonance from the inverse opal, surface plasmon resonance is greatly improved in this photonic scaffold, leading to a photocurrent of 3.1 mA cm^{-2} that is about 4 times higher than that of the planar film.

A scaffold consisting of two functional structures (*i.e.*, TiO_2 NRs plus inverse opal layers) has been designed for supporting Au NPs (Fig. 8f). By optimizing the pore size of inverse opals, the photonic bandgap is tuned to match the plasmonic resonance band of gold NPs. Hereby, more hot-electrons from gold NPs are transferred to the TiO_2 conductive band, leading to an improved PEC performance with a photoconversion efficiency of 0.71.[112]

Plasmonic particles plus QDs as dual sensitizers on photonic structures have been built to boost the efficiency.[43,112–114] These 3D-heterogeneous inverse opals offer a large surface area for loading both metal particles and quantum-dot sensitizers (Fig. 9a and b), exposing abundant active-sites for the reaction. The charge transfer mechanism of the structure is explained in Fig. 9c. Under irradiation, ZnO inverse opal and quantum-dot sensitizers are simultaneously excited and produce charge carriers. The decorated gold NPs function as a bridge for transferring the electrons from CdS to the conductive band of ZnO. At the same time, plasmon-induced hot electrons from Au NPs also inject into the conduction band. Thus, the combined effects increase charge transport and photon absorption, producing a photocurrent density of 5.7 mA cm^{-2}. This photocurrent is much larger than that of the Au NPs doped sample, ~0.85 mA cm^{-2}, and CdS sensitized sample, ~2.5 mA cm^{-2} (Fig. 9d).[114] These results suggest that a combination of plasmonic metals with photonic crystals brings a synergistic effect and amplifies the corresponding PEC performance.

4. Summary and prospects

This work summarizes the physical understanding and structural design of plasmonic photoelectrodes, and illustrates their key features for solar water splitting. Particularly, we focus our discussion on three essential heterostructures: planar thin
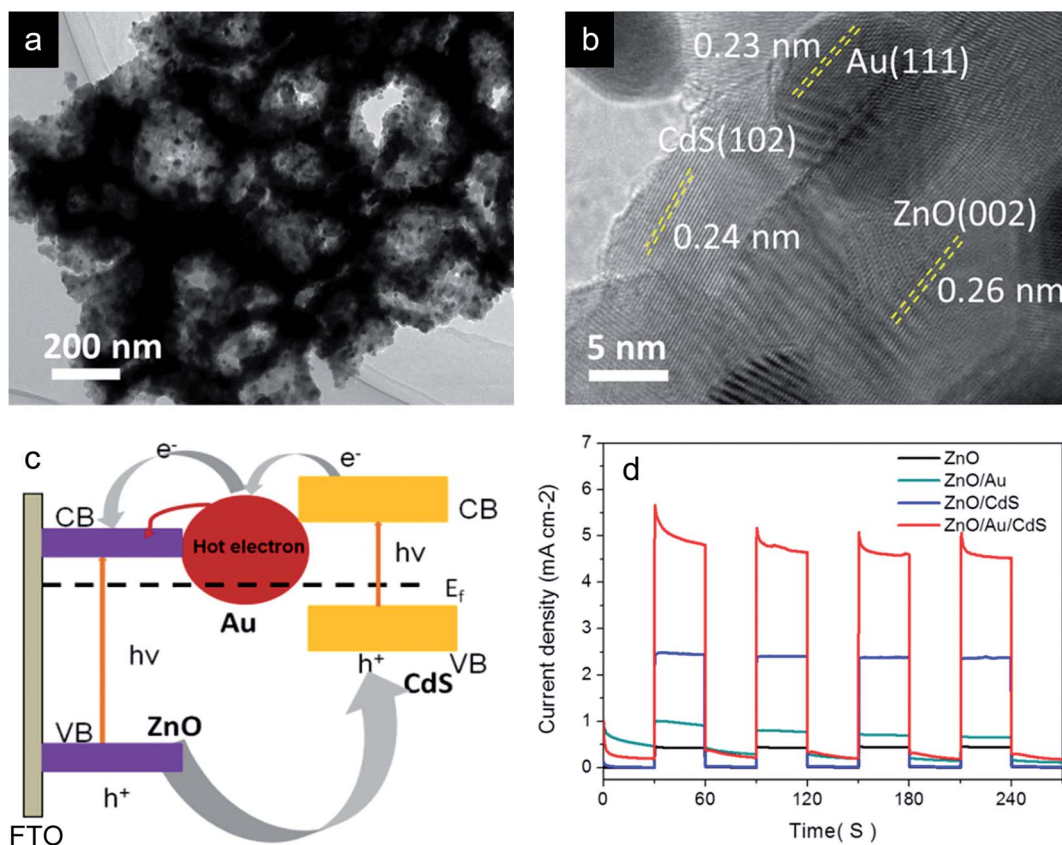

Fig. 9 (a) TEM image of Au NPs–ZnO inverse opals and (b) HRTEM image of Au/CdS–ZnO inverse opals. (c) Charge transport in the ZnO/Au/CdS photoelectrode and (d) *I*–*t* curves of the different photoanodes. Reproduced with permission.[114] Copyright 2015 Wiley-VCH.

Table 1 Summary of the planar thin film PPEs and their PEC performance

Materials	Substrate	Preparation methods	Dielectric layer	Plasmon-assembling	Structure	Annealing (°C)	Photocurrent (mA cm^{-2})	Test conditions AM1.5 100 mW cm^{-2}	Stability	Feature	Ref.
Au NPs/NiO$_x$/Al	Al/Si	Spin-coating	NiO$_x$	e-Beam evaporation	Embedded	300	25 μA cm^{-2}	0 V$_{RHE}$ 0.5 M Na$_2$SO$_4$	NA	10 and 30 nm Au NPs 40 nm NiO$_x$ layer 200 nm Al/Si substrate	29
Au NPs/TiO$_2$	FTO	RF sputtering	—	RF sputtering	Embedded	400	2.3 μA cm^{-2}	1 M KOH 70 mW cm^{-2}, λ > 550 nm	NA	5–20 nm Au NPs 100 nm thickness	31
Au–Ag alloy NPs/TiO$_2$	Glassy slides and Ti	RF sputtering	—	RF sputtering	Embedded	600	5.9	0.5 V$_{Ag/AgCl}$ 1 M KOH	NA	Alloy NPs ~40–100 nm thickness	37
Au NPs/WO$_3$	FTO	Doctor blade	—	Drop-coating	Embedded	300	0.44	1 V$_{Ag/AgCl}$ 0.5 M NaSO$_4$	NA	10 nm Au NPs 60–80 nm WO$_3$ NPs	33
Au NPs/BiVO$_4$	FTO	Dip-coating	—	Dropcast	Embedded	500	1.2	0.5 V$_{Ag/AgCl}$ aqueous phosphate	4 h 90%	10–80 nm Au NPs 10–300 nm BiVO$_4$	34
Au NPs/TiO$_2$	FTO	RF sputtering	—	Direct current sputtering	Buried	600	1.8 μA cm^{-2}	0.2 V$_{Ag/AgCl}$ methanol% = 25%	NA	20–50 nm Au NPs ~300 nm thickness	39
Au NPs/Fe$_2$O$_3$	TiO$_2$/FTO	Spin-coating CVD	—	Electrodeposition	Buried	500	0.58	0.6 V$_{Ag/AgCl}$ 0.5 M NaOH	NA	70–80 nm Au NPs 110–650 nm thickness	40
Ag film/Cu$_2$O/ZnO	ITO	Electrochemical deposition ALD	—	Vacuum evaporation	Buried	180	1.1	1 V$_{Ag/AgCl}$ 0.5 M NaSO$_4$	NA	50 nm Ag layer 50 nm Al–ZnO film 180 nm Cu$_2$O	41
Ag NPs@TiO$_2$	ITO	Drop-coating	—	Hydrothermal	Isolated	400	0.25	0.2 V$_{Ag/AgCl}$ 0.1 M HNO$_3$ or 0.1 M NaOH λ = 400 nm 79.3 mW cm^{-2}	NA	6.5 nm Ag NPs 2.59 nm TiO$_2$ shell Ag@TiO$_2$ 2.0 μm thickness	42
Au@TiO$_2$/CuWO$_4$	FTO	Spray deposition	—	Electrostatic precipitation	Isolated	500	0.1	1.23 V$_{RHE}$ K$_2$HPO$_4$	NA	35 nm Au NPs 2 nm TiO$_2$ shell 235 nm thickness	46
Au@SiO$_2$/Fe$_2$O$_3$	ITO FTO	e-Beam evaporation	SiO$_2$	Dropcast	Isolated	600	2	1.41 V$_{RHE}$ water with 0.2 M sodium acetate	NA	Au NPs 50 nm SiO$_2$ shell 10 nm 100 nm thickness	54
Ag NPs@SiO$_2$/BiVO$_4$	FTO	Spray pyrolysis	SiO$_2$	Doctor blade	Isolated	450	1.6	1.23 V$_{RHE}$ 0.1 M K$_2$HPO$_4$	25 minutes	50 nm Ag NPs 10 nm SiO$_2$ shell 100 nm thickness	55
Au NPs@polyoxometalate NPs/WO$_3$	FTO	Sol–gel	Polyoxometalate	Surface decoration	Isolated	500	1.8	1.2 V$_{RHE}$ 1 M H$_2$SO$_4$ or 1 M CH$_3$SO$_3$H	NA	30–40 nm Au NPs 400 nm thickness	48
Ag nanocubes@-polyvinyl pyrrolidone/N-TiO$_2$	ITO	Drop-coating	Polyvinyl-pyrrolidone	Mixing and sonicating	Isolated	500	2.5 μA cm^{-2}	0.3 V$_{Hg/Hgo}$ 1 M KOH	NA	Ag nanocubes 120 nm Au NPs 24.5 nm 750 nm thickness	47
1 wt% Au NPs@TiO$_2$/Al$_2$O$_3$/Cu$_2$O	FTO	Doctor-blade	Al$_2$O$_3$	Spin-coating	Isolated	450	4.34	0.2 V$_{Ag/AgCl}$ 0.1 M NaSO$_4$	5 h	37, 70, 100, 120 nm Au NPs 8 μm thickness	56

Table 2 Summary of the 1D nanowire/rod PPEs and their PEC performance

Materials	Substrate	Preparation methods	Dielectric layer	Plasmon-assembling	Structure	Annealing (°C)	Photocurrent (mA cm^{-2})	Test conditions AM1.5 100 mW cm^{-2}	Stability	Feature	Ref.
Co-OEC/AuNR/TiO$_2$	ITO	Electron-beam evaporation	—	Electrodeposition	Pure metal	500	0.35	0.5 V_{RHE} one molar potassium borate	NA	~90 nm Au NR array 20 nm TiO$_2$ layer	59
Pt/TiO$_2$/Au NRs	ITO	Electron-beam evaporation/ALD	—	Electrodeposition	Pure metal	—	18 µA cm^{-2}	0 V_{NHE} 1 M Na$_2$SO$_4$	60 h	90–100 nm Au NR array 5–20 nm TiO$_2$ layer ~20 nm Co-OEC thickness	58
TiO$_2$/Au nanodots	ITO	Dip-coating	—	e-Beam evaporation	Pure metal	300	4 µA cm^{-2}	0.397 V_{SHE} 0.1 M KOH 122.5 mW cm^{-2}	40 h	50, 63, and 83 nm dot size nanodot with 110 nm of TiO$_2$ overcoats	60
Ag NWs@perylene	ITO	Dropcast	Perylene	Hydrothermal	Pure metal	60	0.8 µA cm^{-2}	−0.2 $V_{Ag/AgCl}$ 0.1 M NaSO$_4$	NA	2.1–8.5 nm shell thickness 40 nm Ag NWs	61
Au NPs/TiO$_2$ NWs	FTO	Hydrothermal	—	Photochemical graft	Embedded	—	1 µA cm^{-2}	1.2 V_{RHE} 1 M NaOH	5 h	2.2 µm thickness	62
Au NPs and/or NRs/TiO$_2$ NWs	FTO	Hydrothermal	—	Dip-coating	Embedded	300	1.49	0 $V_{Ag/AgCl}$ 1 M NaOH	NA	8 nm Au NPs 40 nm length and 15 nm width Au NRs	63
Au NPs/ZnO NWs	FTO	Hydrothermal	—	Chemical deposition	Embedded	450	1.3	1 $V_{Ag/AgCl}$ 0.5 M Na$_2$SO$_4$	3 h	4.7 nm Au NPs ~5 µm thickness	66
Au NPs/ZnO NWs	Zn	Hydrothermal	—	Photodeposition reduction	Embedded	180	9.11	1 $V_{Ag/AgCl}$ 0.1 M Na$_2$SO$_4$	NA	6.5 nm Au NPs 300–400 nm ZnO diameter ~4 µm thickness	65
Ag nanoprisms/ZnO NRs	ITO	Hydrothermal	—	Spin-coating	Embedded	500	2.3	1 $V_{Ag/AgCl}$ 0.5 M Na$_2$SO$_4$ 60 mW cm^{-2}	50 min	30–100 nm Ag nanoprisms	67
Ag film/ZnO NRs	Polyethylene terephthalate	Hydrothermal	—	e-Beam evaporation	Embedded	90	2.25	1 $V_{Ag/AgCl}$ 0.5 M Na$_2$SO$_4$	NA	10 nm Ag films 100–200 nm ZnO diameter ~2 µm thickness flexible substrate bent to $R = 6.0$ mm	68
Au NPs/Fe$_2$O$_3$ nanoplatelets	FTO	Ultrasonic spray pyrolysis	—	Thermophoresis deposition	Embedded or buried	550	2.0	1.4 $V_{Ag/AgCl}$ 1 M Na$_2$SO$_4$	NA	50 nm Au NPs 300 nm thickness	26

Table 2 (Contd.)

Materials	Substrate	Preparation methods	Dielectric layer	Plasmon-assembling	Structure	Annealing (°C)	Photocurrent (mA cm^{-2})	Test conditions AM1.5 100 mW cm^{-2}	Stability	Feature	Ref.
Fe$_2$O$_3$ NW/Au nanoholes	FTO	Hydrothermal	—	Lithography	Embedded	650	0.95	0.23 V$_{Ag/AgCl}$ 1 M NaOH	NA	Au nanoholes are 85 nm high and 350 nm in diameter 150 nm long Fe$_2$O$_3$ NW	69
ZnS–Ag–CdS–Au–CdSe nanobamboo	ITO	Electrodeposition	—	Electrodeposition	Embedded	120	4.75	0 V$_{Ag/AgCl}$ 0.2 M Na$_2$S/ 1 M Na$_2$SO$_3$	0.5 h	Individual NR is ~200 nm in diameter 1.5 μm in length	70
Au NPs/ Zn$_x$Cd$_{1-x}$Se$_y$Te$_{1-y}$/ ZnO NWs	ITO	Hydrothermal	—	Spin coating	Embedded	120	19.63 μA cm^{-2}	0 V$_{SCE}$ 0.1 M Na$_2$SO$_4$ 377 mW cm^{-2}	12 h	~10 nm Au NPs 10 nm shell thickness 150 nm ZnO diameter	75
Au NPs/ZnS/ZnO NWs	FTO	Hydrothermal	—	Photodeposition reduction	Embedded	350	0.58	1 V$_{Ag/AgCl}$ 0.5 M Na$_2$SO$_4$ 50 mW cm^{-2} white light	NA	200 nm ZnO NW 5 μm thickness	76
AgNPs/ polydopamine (PDA)/ZnO NWs	FTO	Hydrothermal	—	Dip/redox	Embedded	350	3.07	1 V$_{Ag/AgCl}$ 0.5 M Na$_2$SO$_4$	30 min	100 nm ZnO NW 5–8 nm shell thickness 1 μm thickness	77
AgNPs/PEDOT/Si NWs	Si	Metal-catalyzed etching	—	Chemical deposition	Embedded	—	6.5	0.5 V$_{SCE}$ water/ methanol	NA	6 nm Ag NPs 2.6 nm shell thickness 11 μm thickness	78
Ag nanoclusters/ ZnO NWs	Ti	Electrodeposition	—	Electrodeposition	Embedded	—	0.17	1.23 V$_{RHE}$ 1 M KOH	NA	20 nm diameter and 100 nm length Ag nanoclusters 1.5–2.0 μm thickness	84
Ag nanoclusters/Si microwires	Si	Dry etching	—	Dropcasting	Embedded	500	−35	−1 V$_{Ag/AgCl}$ 0.5 M Na$_2$SO$_4$	NA	20–100 nm Ag nanoclusters 850 nm Si NW 1–12 μm thickness	85
AuNPs/branched-ZnO NWs	FTO	Hydrothermal	—	Ion sputtering	Embedded	500	1.45	1 V$_{RHE}$ 0.5 M Na$_2$SO$_4$	NA	~8 nm Au NPs ~200 nm lengths, ~30 nm diameter of ZnO secondary branches 50–200 nm ZnO NW 9 μm thickness	86

Table 2 (*Contd.*)

Materials	Substrate	Preparation methods	Dielectric layer	Plasmon-assembling	Structure	Annealing (°C)	Photocurrent (mA cm^{-2})	Test conditions AM1.5 100 mW cm^{-2}	Stability	Feature	Ref.
Ag/Ag$_2$S/Ag$_3$CuS$_2$/TiO$_2$ NRs	FTO	Hydrothermal	—	Dip-coating	Embedded	150	9.82	0.47 V$_{Ag/AgCl}$ 1 M NaOH	NA	~60 nm diameter TiO$_2$ NW	87
Au NPs/ZnO NRs@NPs	FTO	Hydrothermal	—	Photo-reduction	Embedded	350	1.47	0.6 V$_{Hg/Hg_2Cl_2}$ 0.5 M Na$_2$SO$_4$	NA	~5 nm Au NPs 30–40 nm nanoplatelet ~90 nm diameter of ZnO NW 3.6 μm thickness	92
Au/UCNs/CdTe/ZnO NRs	FTO	Hydrothermal	—	Dip-coating	Embedded	450	0.036	1 V$_{Ag/AgCl}$ 0.5 M Na$_2$SO$_4$ 980 nm laser	2 h	30–35 nm UCNs ~150 nm diameter ZnO NW 5 μm thickness	91
CdS/Au NPs/TiO$_2$ NRs	FTO	Hydrothermal	—	Dip-coating	Buried	450	4.07	0 V$_{Ag/AgCl}$ 0.25 M Na$_2$S and 0.35 M Na$_2$SO$_3$	NA	11 nm Au NPs 150–200 nm TiO$_2$ NRs 15 nm CdS shell thickness 2.5 μm thickness	79
CdS/Ag NPs/ZnO NWs	ITO	Hydrothermal	—	Dip-coating	Buried	90	1.5	0.4 V$_{Ag/AgCl}$ 0.25 M Na$_2$S and 0.35 M Na$_2$SO$_3$ 60 mW cm^{-2}	10 h	10–30 nm Ag NPs ~1.5 μm thickness	81
Al$_2$O$_3$/AuNPs/Fe$_2$O$_3$ NWs	FTO	Electrodeposition	Al$_2$O$_3$	Ion sputtering	Buried	300	0.75	0.4 V$_{Ag/AgCl}$ 1 M KOH	NA	2–40 nm Au NPs 40 nm Fe$_2$O$_3$ NRs ~1.2 μm thickness	82
Ag@Ag$_2$S NPs/TiO$_2$ NWs	Ti	Hydrothermal	Ag$_2$S	Dip-coating	Isolated	450	39 μA cm^{-2}	0.2 V$_{Ag/AgCl}$ 0.1 M NaOH	NA	25 nm Ag@Ag$_2$S NPs	71
Au@SiO$_2$/TiO$_2$	FTO	Hydrothermal	SiO$_2$	Dropcasting	Isolated	500	0.92	0.7 V$_{SCE}$ 0.5 M Na$_2$SO$_4$	NA	120 nm Au@SiO$_2$ NPs	72
Ag@Ag$_3$(PO$_4$)$_{1-x}$ NPs/ZnO NWs	ITO	Electrodeposition	Ag$_3$(PO$_4$)$_{1-x}$	Electrochemical deposition	Isolated	300	3.1	0.6 V$_{Pt}$ 0.5 M Na$_2$SO$_4$	10 h	8 nm Ag$_3$(PO$_4$)$_{1-x}$ NPs ~250 nm ZnO NW diameter	73
Au@SiO$_2$ NPs/Cu$_2$O NWs	FTO	Drop-casting	SiO$_2$	Drop-casting	Isolated	120	42 μA cm^{-2}	0 V$_{RHE}$ 0.1 M Na$_2$SO$_4$ 300 mW cm^{-2}	20 min	~10 nm Au NPs 5–20 nm SiO$_2$ shells 1–5 μm thickness	74

Table 3 Summary of the porous PPEs and their PEC performance

Materials	Substrate	Preparation methods	Dielectric layer	Plasmon-assembling	Structure	Annealing (°C)	Photocurrent (mA cm^{-2})	Test conditions AM1.5 100 mW cm^{-2}	Stability	Feature	Ref.
Au/TNTs	FTO	Hydrothermal	—	Seed solution growth	Embedded	380	42 μA cm^{-2}	0.5 M methanol + 0.5 M KOH	NA	30–100 nm Au NPs	95
Au/TNTs	Ti	Anodization	—	e-Beam evaporation	Embedded	400	—	1 M KOH λ = 633 nm 150 mW cm^{-2}	NA	40 nm diameter of TNTs	97
Au/TNTs	Ti	Anodization	—	Pulse electrodeposition	Embedded	500	8 μA cm^{-2}	0.6 V_{SHE} 0.1 M Na$_2$SO$_4$ λ > 420 nm	NA	8–40 nm Au NPs 100 nm diameter of TNTs 1.0 μm thickness	96
Au/RGO/H-TNTs	Ti	Anodization	—	Electrophoretic deposition	Embedded	450	0.224	1.23 V_{RHE} 1 M KOH λ > 400 nm	NA	25 nm Au NPs 145 nm diameter of TNTs 12 μm thickness	98
Ag/TNTs	Ti	Anodization	—	Pulse electrodeposition	Embedded	500	0.104	0.7 V_{SHE} 0.5 M Na$_2$SO$_4$ λ > 420 nm	NA	1.3–21 nm Ag NPs 43 nm inner diameter of TNTs 2.0 μm thickness	99
Ag/N-TNTs	Ti	Anodization	—	Electrochemical deposition	Embedded	450	0.14	1.23 V_{RHE} 1 M KOH	NA	5 nm Ag NPs 30 nm inner diameter of TNTs 3.0 μm thickness	100
Au/TNT-PCs	Ti	Anodization	—	Photocatalytic reduction deposition	Embedded	500	2.25	1.23 V_{RHE} 1 M KOH entire solar light irradiation	2 h	20 nm Au NPs 200 nm diameter of TNTs 2.0 μm thickness	104
Au$_x$/Au/TNT-PCs	Ti	Anodization	—	Layer by layer self-assembly	Embedded	450	68 μA cm^{-2}	0.1 M Na$_2$S	NA	90 nm inner diameter of TNTs 9.0 μm thickness	105
Au NPs/TiO$_2$ NPs	FTO	Screen-printing	—	Ionic adsorption/reduction	Embedded	450	20 μA cm^{-2}	0.02 V_{RHE} 1 M NaOH	NA	9 nm Au NPs 15 nm TiO$_2$ NPs ~5.0 μm thickness	108
Au NPs/TiO$_2$ inverse opal	FTO	Infiltration	—	Dip-coating	Embedded	500	0.8	0.5 $V_{Ag/AgCl}$ 0.24 M Na$_2$S and 0.35 M Na$_2$SO$_3$	NA	30 nm Au NPs 290 nm diameter of inverse opal ~2.4 μm thickness	110
Au NPs/BiVO$_4$ inverse opal	FTO	Dip-coating infiltration	—	Dropcasting	Embedded	500	3.1	1.23 V_{RHE} 0.1 M phosphate solution	NA	20 nm Au NPs 200 nm diameter of inverse opal ~1.5 μm thickness	111
CdS/Au/ZnO inverse opal	FTO	Atomic layer deposition	—	Ionic adsorption and reduction	Embedded	450	5.7	0 $V_{Ag/AgCl}$ 0.25 M Na$_2$S and 0.35 M Na$_2$SO$_3$	5000 s	10 nm Au NPs 200 nm diameter of inverse opal ~3.0 μm thickness	114
Au/TiO$_2$ NR-PCs	FTO	Hydrothermal	—	Ionic adsorption and reduction	Embedded	450	1.6	1 V_{RHE} 1 M KOH	NA	10 nm Au NPs 250 nm diameter of inverse opal 5.0–6.0 μm thickness	112
AgBr@Ag/TNTs	Ti	Anodization	—	Ionic layer adsorption/reaction	Isolated	450	0.73	0.25 V bias 0.1 M Na$_2$S and 0.1 M Na$_2$SO$_3$	NA	50–300 nm AgBr@Ag NPs 165 nm diameter of TNTs	101
Al$_2$O$_3$/Au/TNTs	Ti	Anodization	Al$_2$O$_3$	Photoreduction deposition	Isolated	450	0.70	0 $V_{Ag/AgCl}$ 1 M KOH	5000 s	16–25 nm Au NPs 2.6 nm Al$_2$O$_3$ layer 87 nm inner diameter of TNTs	103

films, nanowire/rod arrays and porous structures. Many intriguing examples have been selected to demonstrate these configurations, which include the pure metal form, embedded form, buried as well as isolated form. The preparation methods, structural configuration of the electrodes and their water-splitting properties are summarized in Tables 1–3. In general, many aspects have been considered for designing an efficient photoelectrode such as the shape or size of plasmonic metals, plasmon–semiconductor interface, film thickness, surface roughness, annealing temperatures and contact status between materials, passive or dielectric layer and stability in electrolytes. A framework has been established to guide the design of electrodes. By judiciously coupling metallic nanomaterials with photoconductive materials, the photocurrent is enhanced to hundred times. However, we have to face trade-offs in many situations, such as shortening the charge-transfer path and enhancing carrier transport, coating a passive layer with retention of electrical contact between materials, *etc.*

Future prospects are likely to focus on clarifying the physical mechanisms in detail to distinguish the dominating parameters in related systems. In addition to the basic understanding of plasmonic water splitting, a novel concept design, controlled synthesis and assembly of the structures are interesting aspects to be explored. Advanced manufacturing processes such as wet-chemical synthesis, low-cost materials deposition and large scale self-assembly are required to meet the technology goals. More techniques for *in situ* characterization should be carried out to predict the experimental results. The unified models that can describe complex interactions between the components are urgently to be mapped. Since there is much scope for plasmon–semiconductor systems, we expect that remarkable advances can be accomplished in the coming years to promote their further commercial applications.

Acknowledgements

References

1 S. J. A. Moniz, S. A. Shevlin, D. J. Martin, Z. X. Guo and J. Tang, *Energy Environ. Sci.*, 2015, **8**, 731–759.

2 A. Fujishima and K. Honda, *Nature*, 1972, **238**, 37–38.

3 S. Cho, J.-W. Jang, K. H. Lee and J. S. Lee, *APL Mater.*, 2014, **2**, 010703.

4 P. Zhang, L. Gao, X. Song and J. Sun, *Adv. Mater.*, 2015, **27**, 562–568.

5 M. L. Brongersma, Y. Cui and S. Fan, *Nat. Mater.*, 2014, **13**, 451–460.

6 E. J. Crossland, N. Noel, V. Sivaram, T. Leijtens, J. A. Alexander-Webber and H. J. Snaith, *Nature*, 2013, **495**, 215–219.

7 K. Ueno, T. Oshikiri and H. Misawa, *ChemPhysChem*, 2016, **17**, 199–215.

8 C. Clavero, *Nat. Photonics*, 2014, **8**, 95–103.

9 P. Christopher, H. Xin, A. Marimuthu and S. Linic, *Nat. Mater.*, 2012, **11**, 1044–1050.

10 R. Jiang, B. Li, C. Fang and J. Wang, *Adv. Mater.*, 2014, **26**, 5274–5309.

11 S. C. Warren and E. Thimsen, *Energy Environ. Sci.*, 2012, **5**, 5133–5146.

12 P. Zhang, T. Wang and J. Gong, *Adv. Mater.*, 2015, **27**, 5328–5342.

13 J. Z. Z. Ying-Chih and Pu. Austin, *J. Nanomed. Nanotechnol.*, 2014, **2**(5), 1030.

14 X. Zhang, Y. L. Chen, R. S. Liu and D. P. Tsai, *Rep. Prog. Phys.*, 2013, **76**, 046401.

15 G. Baffou and R. Quidant, *Chem. Soc. Rev.*, 2014, **43**, 3898–3907.

16 S. Linic, P. Christopher and D. B. Ingram, *Nat. Mater.*, 2011, **10**, 911–921.

17 W. R. Erwin, H. F. Zarick, E. M. Talbert and R. Bardhan, *Energy Environ. Sci.*, 2016, **9**, 1577–1601.

18 C. Jia, X. Li, N. Xin, Y. Gong, J. Guan, L. Meng, S. Meng and X. Guo, *Adv. Energy Mater.*, 2016, **6**, 1600431.

19 H. Tuysuz and C. K. Chan, *Top. Curr. Chem.*, 2016, **371**, 215–252.

20 K. Wu, J. Chen, J. R. McBride and T. Lian, *Science*, 2015, **349**, 632–635.

21 L. Zhou, Y. Tan, J. Wang, W. Xu, Y. Yuan, W. Cai, S. Zhu and J. Zhu, *Nat. Photonics*, 2016, **10**, 393–398.

22 M. Gao, P. K. N. Connor and G. W. Ho, *Energy Environ. Sci.*, 2016, **9**, 3151–3160.

23 J. Li, S. K. Cushing, F. Meng, T. R. Senty, A. D. Bristow and N. Wu, *Nat. Photonics*, 2015, **9**, 601–607.

24 S. Mukherjee, L. Zhou, A. M. Goodman, N. Large, C. Ayala-Orozco, Y. Zhang, P. Nordlander and N. J. Halas, *J. Am. Chem. Soc.*, 2014, **136**, 64–67.

25 M. J. Kale, T. Avanesian and P. Christopher, *ACS Catal.*, 2014, **4**, 116–128.

26 E. Thimsen, F. Le Formal, M. Gratzel and S. C. Warren, *Nano Lett.*, 2011, **11**, 35–43.

27 X. Liu, J. Iocozzia, Y. Wang, X. Cui, Y. Chen, S. Zhao, Z. Li and Z. Lin, *Energy Environ. Sci.*, 2016, **9**, 2511–2532.

28 Y. Tian and T. Tatsuma, *J. Am. Chem. Soc.*, 2005, **127**, 7632–7637.

29 H. Robatjazi, S. M. Bahauddin, C. Doiron and I. Thomann, *Nano Lett.*, 2015, **15**, 6155–6161.

30 S. Linic, U. Aslam, C. Boerigter and M. Morabito, *Nat. Mater.*, 2015, **14**, 567–576.

31 W. Chen, Y. Lu, W. Dong, Z. Chen and M. Shen, *Mater. Res. Bull.*, 2014, **50**, 31–35.

32 N. Naseri, M. Qorbani, H. Kim, W. Choi and A. Z. Moshfegh, *J. Phys. Chem. C*, 2015, **119**, 1271–1279.

33 F. Xu, Y. Yao, D. Bai, R. Xu, J. Mei, D. Wu, Z. Gao and K. Jiang, *RSC Adv.*, 2015, **5**, 60339–60344.

34 L. Zhang, L. O. Herrmann and J. J. Baumberg, *Sci. Rep.*, 2015, **5**, 16660.

35 D. Kim, J. Resasco, Y. Yu, A. M. Asiri and P. Yang, *Nat. Commun.*, 2014, **5**, 4948.

36 M. Kotesh Kumar, K. Bhavani, G. Naresh, B. Srinivas and A. Venugopal, *Appl. Catal., B*, 2016, **199**, 282–291.

37 N. Naseri, P. Sangpour and S. H. Mousavi, *RSC Adv.*, 2014, **4**, 46697–46703.

38 S. Mubeen, G. Hernandez-Sosa, D. Moses, J. Lee and M. Moskovits, *Nano Lett.*, 2011, **11**, 5548–5552.

39 Z. Zhan, J. An, H. Zhang, R. V. Hansen and L. Zheng, *ACS Appl. Mater. Interfaces*, 2014, **6**, 1139–1144.

40 P. S. Archana, N. Pachauri, Z. Shan, S. Pan and A. Gupta, *J. Phys. Chem. C*, 2015, **119**, 15506–15516.

41 Y. Liu, F. Ren, S. Shen, Y. Fu, C. Chen, C. Liu, Z. Xing, D. Liu, X. Xiao, W. Wu, X. Zheng, Y. Liu and C. Jiang, *Appl. Phys. Lett.*, 2015, **106**, 123901.

42 H.-Y. Chuang and D.-H. Chen, *Int. J. Hydrogen Energy*, 2011, **36**, 9487–9495.

43 S. Yu, Y. H. Kim, S. Y. Lee, H. D. Song and J. Yi, *Angew. Chem.*, 2014, **53**, 11203–11207.

44 R. Sellappan, M. G. Nielsen, F. González-Posada, P. C. K. Vesborg, I. Chorkendorff and D. Chakarov, *J. Catal.*, 2013, **307**, 214–221.

45 A. Sousa-Castillo, M. Comesaña-Hermo, B. Rodríguez-González, M. Pérez-Lorenzo, Z. Wang, X.-T. Kong, A. O. Govorov and M. A. Correa-Duarte, *J. Phys. Chem. C*, 2016, **120**, 11690–11699.

46 M. Valenti, D. Dolat, G. Biskos, A. Schmidt-Ott and W. A. Smith, *J. Phys. Chem. C*, 2015, **119**, 2096–2104.

47 D. B. Ingram and S. Linic, *J. Am. Chem. Soc.*, 2011, **133**, 5202–5205.

48 R. Solarska, K. Bienkowski, S. Zoladek, A. Majcher, T. Stefaniuk, P. J. Kulesza and J. Augustynski, *Angew. Chem.*, 2014, **53**, 14196–14200.

49 J. F. Li, Y. F. Huang, Y. Ding, Z. L. Yang, S. B. Li, X. S. Zhou, F. R. Fan, W. Zhang, Z. Y. Zhou, Y. Wu de, B. Ren, Z. L. Wang and Z. Q. Tian, *Nature*, 2010, **464**, 392–395.

50 C. Hagglund, G. Zeltzer, R. Ruiz, I. Thomann, H. B. Lee, M. L. Brongersma and S. F. Bent, *Nano Lett.*, 2013, **13**, 3352–3357.

51 K. Awazu, M. Fujimaki, C. Rockstuhl, J. Tominaga, H. Murakami, Y. Ohki, N. Yoshida and T. Watanabe, *J. Am. Chem. Soc.*, 2008, **130**, 1676–1680.

52 N. Zhang, C. Han, Y.-J. Xu, J. J. Foley Iv, D. Zhang, J. Codrington, S. K. Gray and Y. Sun, *Nat. Photonics*, 2016, **10**, 473–482.

53 J. Chen, C.-L. Dong, Y. Du, D. Zhao and S. Shen, *Adv. Mater. Interfaces*, 2015, **2**, 1500280.

54 I. Thomann, B. A. Pinaud, Z. Chen, B. M. Clemens, T. F. Jaramillo and M. L. Brongersma, *Nano Lett.*, 2011, **11**, 3440–3446.

55 F. F. Abdi, A. Dabirian, B. Dam and R. van de Krol, *Phys. Chem. Chem. Phys.*, 2014, **16**, 15272–15277.

56 P. Peerakiatkhajohn, T. Butburee, J.-H. Yun, H. Chen, R. M. Richards and L. Wang, *J. Mater. Chem. A*, 2015, **3**, 20127–20133.

57 H. Chen, L. Shao, Q. Li and J. Wang, *Chem. Soc. Rev.*, 2013, **42**, 2679–2724.

58 S. Mubeen, J. Lee, N. Singh, S. Kramer, G. D. Stucky and M. Moskovits, *Nat. Nanotechnol.*, 2013, **8**, 247–251.

59 J. Lee, S. Mubeen, X. Ji, G. D. Stucky and M. Moskovits, *Nano Lett.*, 2012, **12**, 5014–5019.

60 H. J. Kim, S. H. Lee, A. A. Upadhye, I. Ro, M. I. Tejedor-Tejedor, M. A. Anderson, W. B. Kim and G. W. Huber, *ACS Nano*, 2014, **8**, 10756–10765.

61 L. Lin, G.-Q. Gao, Q. Zhu and A.-W. Xu, *J. Mater. Chem. A*, 2015, **3**, 12845–12851.

62 J. S. DuChene, B. C. Sweeny, A. C. Johnston-Peck, D. Su, E. A. Stach and W. D. Wei, *Angew. Chem.*, 2014, **53**, 7887–7891.

63 Y. C. Pu, G. Wang, K. D. Chang, Y. Ling, Y. K. Lin, B. C. Fitzmorris, C. M. Liu, X. Lu, Y. Tong, J. Z. Zhang, Y. J. Hsu and Y. Li, *Nano Lett.*, 2013, **13**, 3817–3823.

64 T.-H. Yang, Y.-W. Harn, M.-Y. Pan, L.-D. Huang, M.-C. Chen, B.-Y. Li, P.-H. Liu, P.-Y. Chen, C.-C. Lin, P.-K. Wei, L.-J. Chen and J.-M. Wu, *Appl. Catal., B*, 2016, **181**, 612–624.

65 M. Wu, W. J. Chen, Y. H. Shen, F. Z. Huang, C. H. Li and S. K. Li, *ACS Appl. Mater. Interfaces*, 2014, **6**, 15052–15060.

66 H. M. Chen, C. K. Chen, C. J. Chen, L. C. Cheng, P. C. Wu, B. H. Cheng, Y. Z. Ho, M. L. Tseng, Y. Y. Hsu, T. S. Chan, J. F. Lee, R. S. Liu and D. P. Tsai, *ACS Nano*, 2012, **6**, 7362–7372.

67 X. Zhang, J. Zhao, S. Wang, H. Dai and X. Sun, *Int. J. Hydrogen Energy*, 2014, **39**, 8238–8245.

68 Y. Wei, L. Ke, J. Kong, H. Liu, Z. Jiao, X. Lu, H. Du and X. W. Sun, *Nanotechnology*, 2012, **23**, 235401.

69 J. Li, S. K. Cushing, P. Zheng, F. Meng, D. Chu and N. Wu, *Nat. Commun.*, 2013, **4**, 2651.

70 X. Wang, C. Liow, A. Bisht, X. Liu, T. C. Sum, X. Chen and S. Li, *Adv. Mater.*, 2015, **27**, 2207–2214.

71 Z. Shan, D. Clayton, S. Pan, P. S. Archana and A. Gupta, *J. Phys. Chem. B*, 2014, **118**, 14037–14046.

72 J. Chen, M. Yu, Y. Wang, S. Shen, M. Wang and L. Guo, *Chin. Sci. Bull.*, 2014, **59**, 2191–2198.

73 Y. G. Lin, Y.-K. Hsu, Y. C. Chen, S. B. Wang, J. T. Miller, L. C. Chen and K. H. Chen, *Energy Environ. Sci.*, 2012, **5**, 8917.

74 J. S. DuChene, B. P. Williams, A. C. Johnston-Peck, J. Qiu, M. Gomes, M. Amilhau, D. Bejleri, J. Weng, D. Su, F. Huo, E. A. Stach and W. D. Wei, *Adv. Energy Mater.*, 2016, **6**, 1501250.

75 X. Zhan, Y. Bao, F. Wang, Q. Wang, Z. Cheng, Z. Wang, K. Xu, Z. Fang and J. He, *Appl. Phys. Lett.*, 2015, **106**, 123904.

76 Y. Liu, Y. Gu, X. Yan, Z. Kang, S. Lu, Y. Sun and Y. Zhang, *Nano Res.*, 2015, **8**, 2891–2900.

77 Y. Wei, J. Kong, L. Yang, L. Ke, H. R. Tan, H. Liu, Y. Huang, X. W. Sun, X. Lu and H. Du, *J. Mater. Chem. A*, 2013, **1**, 5045–5052.

78 C. Duan, H. Wang, X. Ou, F. Li and X. Zhang, *ACS Appl. Mater. Interfaces*, 2014, **6**, 9742–9750.

79 J. Li, S. K. Cushing, P. Zheng, T. Senty, F. Meng, A. D. Bristow, A. Manivannan and N. Wu, *J. Am. Chem. Soc.*, 2014, **136**, 8438–8449.

80 W. Fan, C. Chen, H. Bai, B. Luo, H. Shen and W. Shi, *Appl. Catal., B*, 2016, **195**, 9–15.

81 X. Zhang, Y. Li, J. Zhao, S. Wang, Y. Li, H. Dai and X. Sun, *J. Power Sources*, 2014, **269**, 466–472.

82 Y. Liu, Z. Xu, M. Yin, H. Fan, W. Cheng, L. Lu, Y. Song, J. Ma and X. Zhu, *Nanoscale Res. Lett.*, 2015, **10**, 374.

83 S. Ramadurgam, T. G. Lin and C. Yang, *Nano Lett.*, 2014, **14**, 4517–4522.

84 J. Q. Jiao, J. Xia, W. D. Qiu, J. G. Tang, G. R. Li, D. B. Kuang, Y. X. Tong and L. P. Chen, *Electrochim. Acta*, 2014, **136**, 217–222.

85 C. J. Chen, M. G. Chen, C. K. Chen, P. C. Wu, P. T. Chen, M. Basu, S. F. Hu, D. P. Tsai and R. S. Liu, *Chem. Commun.*, 2015, **51**, 549–552.

86 X. Zhang, Y. Liu and Z. Kang, *ACS Appl. Mater. Interfaces*, 2014, **6**, 4480–4489.

87 K. Guo, Z. Liu, J. Han, X. Zhang, Y. Li, T. Hong and C. Zhou, *J. Power Sources*, 2015, **285**, 185–194.

88 Z. Zhang, Y. Huang, K. Liu, L. Guo, Q. Yuan and B. Dong, *Adv. Mater.*, 2015, **27**, 5906–5914.

89 W. Zhu, R. Esteban, A. G. Borisov, J. J. Baumberg, P. Nordlander, H. J. Lezec, J. Aizpurua and K. B. Crozier, *Nat. Commun.*, 2016, **7**, 11495.

90 G. Zhou, X. Xu, T. Ding, B. Feng, Z. Bao and J. Hu, *ACS Appl. Mater. Interfaces*, 2015, **7**, 26819–26827.

91 C. K. Chen, H. M. Chen, C. J. Chen and R. S. Liu, *Chem. Commun.*, 2013, **49**, 7917–7919.

92 C. Zhang, M. Shao, F. Ning, S. Xu, Z. Li, M. Wei, D. G. Evans and X. Duan, *Nano Energy*, 2015, **12**, 231–239.

93 P. Peerakiatkhajohn, J. H. Yun, H. Chen, M. Lyu, T. Butburee and L. Wang, *Adv. Mater.*, 2016, **28**, 6405–6410.

94 Z. Bian, T. Tachikawa, P. Zhang, M. Fujitsuka and T. Majima, *J. Am. Chem. Soc.*, 2014, **136**, 458–465.

95 X. Wu, A. Centeno, X. Zhang, D. Darvill, M. P. Ryan, D. J. Riley, N. M. Alford and F. Xie, *Sol. Energy Mater. Sol. Cells*, 2015, **138**, 80–85.

96 L. Wu, F. Li, Y. Xu, J. W. Zhang, D. Zhang, G. Li and H. Li, *Appl. Catal., B*, 2015, **164**, 217–224.

97 Z. Liu, W. Hou, P. Pavaskar, M. Aykol and S. B. Cronin, *Nano Lett.*, 2011, **11**, 1111–1116.

98 J. Luo, D. Li, Y. Yang, H. Liu, J. Chen and H. Wang, *J. Alloys Compd.*, 2016, **661**, 380–388.

99 Z. Lian, W. Wang, S. Xiao, X. Li, Y. Cui, D. Zhang, G. Li and H. Li, *Sci. Rep.*, 2015, **5**, 10461.

100 J. Jiao, J. Tang, W. Gao, D. Kuang, Y. Tong and L. Chen, *J. Power Sources*, 2015, **274**, 464–470.

101 Q. Wang, J. Qiao, R. Jin, X. Xu and S. Gao, *J. Power Sources*, 2015, **277**, 480–485.

102 Z. W. Seh, S. Liu, M. Low, S. Y. Zhang, Z. Liu, A. Mlayah and M. Y. Han, *Adv. Mater.*, 2012, **24**, 2310–2314.

103 Z. Xu, Y. Lin, M. Yin, H. Zhang, C. Cheng, L. Lu, X. Xue, H. J. Fan, X. Chen and D. Li, *Adv. Mater. Interfaces*, 2015, **2**, 1500169.

104 Z. Zhang, L. Zhang, M. N. Hedhili, H. Zhang and P. Wang, *Nano Lett.*, 2013, **13**, 14–20.

105 F. X. Xiao, Z. Zeng and B. Liu, *J. Am. Chem. Soc.*, 2015, **137**, 10735–10744.

106 X. Zheng and L. Zhang, *Energy Environ. Sci.*, 2016, **9**, 2511–2532.

107 K. Takahiro, S. i. Naya and H. Tada, *J. Phys. Chem. C*, 2014, **118**, 26887–26893.

108 M. Haro, R. Abargues, I. Herraiz-Cardona, J. Martínez-Pastor and S. Giménez, *Electrochim. Acta*, 2014, **144**, 64–70.

109 K. Ji, H. Arandiyan, P. Liu, L. Zhang, J. Han, Y. Xue, J. Hou and H. Dai, *Nano Energy*, 2016, **27**, 515–525.

110 K. Kim, P. Thiyagarajan, H. J. Ahn, S. I. Kim and J. H. Jang, *Nanoscale*, 2013, **5**, 6254–6260.

111 L. Zhang, C. Y. Lin, V. K. Valev, E. Reisner, U. Steiner and J. J. Baumberg, *Small*, 2014, **10**, 3970–3978.

112 X. Zhang, Y. Liu, S. T. Lee, S. Yang and Z. Kang, *Energy Environ. Sci.*, 2014, **7**, 1409.

113 H. Zhao, M. Wu, J. Liu, Z. Deng, Y. Li and B. L. Su, *Appl. Catal., B*, 2016, **184**, 182–190.

114 C. Li, X. Zhu, H. Zhang, Z. Zhu, B. Liu and C. Cheng, *Adv. Mater. Interfaces*, 2015, **2**, 1500428.